Materials & Design 223 (2022) 111223

Contents lists available at ScienceDirect

Materials & Design

journal homepage: www.elsevier.com/locate/matdes

Harnessing structural stochasticity in the computational discovery and design of microstructures

Leidong Xu, Nathaniel Hoffman, Zihan Wang, Hongyi Xu *

Department of Mechanical Engineering, University of Connecticut, 191 Auditorium Road, Storrs, CT 06269, United States

HIGHLIGHTS

- Proposed a property-aware deep generative model to provide a unified design space for stochastic and periodic (deterministic) microstructures.
- Established the first of its kind microstructure database that includes various types of stochastic and periodic structural patterns.
- Proposed a microstructure design approach that tailors structural stochasticity and property simultaneously.
- Created stochastically graded structure designs using microstructure designs with continuously increasing structural stochasticity.

GRAPHICAL ABSTRACT

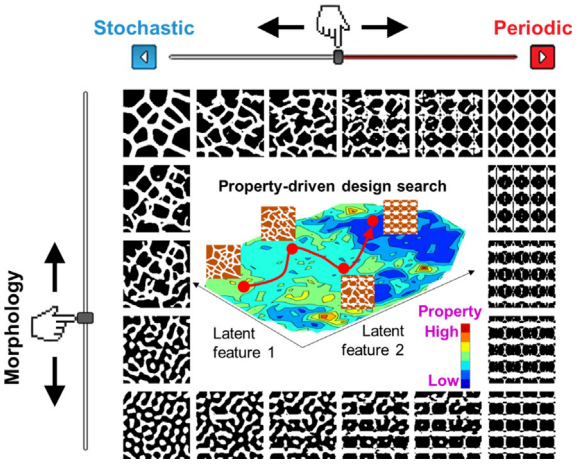

ARTICLE INFO

Article history:
Received 28 June 2022
Revised 19 September 2022
Accepted 2 October 2022
Available online 5 October 2022

Keywords:
Microstructure design
Deep generative model
Stochasticity
Design optimization
Stochastically graded structures

ABSTRACT

This paper presents a deep generative model-based design methodology for tailoring the structural stochasticity of microstructures. Although numerous methods have been established for designing deterministic (periodic) or stochastic microstructures, a systematic design approach that allows the unified treatment of both deterministic and stochastic microstructure design domains has yet to be created. The proposed methodology resolves this issue by learning a unified feature space that embodies diverse structural patterns with continuously varying stochasticity levels. A highly diverse microstructure database is established to incorporate various types of deterministic and stochastic microstructure patterns. A property-aware deep generative model is proposed to learn a unified feature space of the structural characteristics, as well as the relationship between structure features and properties of interest. Autoencoder (AE), Variational Autoencoder (VAE), and Adversarial Autoencoder (AAE) are compared to understand their relative merits in the property-aware learning of the unified feature space. Microstructural designs with tailorable stochasticity and properties are obtained by searching the unified feature space. Multiple design cases are presented to demonstrate the capability of designing microstructures for structural stochasticity and properties. Furthermore, the proposed method is employed to create stochastically graded structures, which manipulate the mechanical behaviors by varying the local stochasticity of the structure.

* Corresponding author.
E-mail address: hongyi.3.xu@uconn.edu (H. Xu).

https://doi.org/10.1016/j.matdes.2022.111223
0264-1275/

1. Introduction

It is known that various levels of stochasticity in structural characteristics (e.g., geometry and material distribution) can be achieved in engineered microstructures. Taking battery electrodes as an example, various fabrication techniques produce microstructures whose stochasticity ranges from random to quasi-regular, such as random particle microstructures by calendaring [1], coral-like quasi-random microstructures by directional ice templating [2], random fiber microstructures by electrospinning [3], and periodic lattices by additive manufacturing (AM) [4]. To design the microstructure of engineered systems, the first step is to define a proper design space that covers all possible design configurations (design representation). However, deterministic (periodic) and stochastic systems lend themselves to distinctively different design representation approaches. In this paper, the term "periodic structure" is used interchangeably with "deterministic structure". The quantitative representation of the deterministic microstructures has been widely studied in the field of structural optimization. Existing representation methods generally fall into two categories: explicit methods and implicit methods [5]. Explicit methods include shape boundary parameterization by analytical functions and splines such as cubic, Akima, Bézier, and NURBS [6–8]. Implicit methods include pixelated/voxelated density fields [9–11] and level set functions [12,13]. For stochastic microstructures, statistical characterization, and stochastic reconstruction (SCSR) methods have been proposed for design representation. Traditional SCSR approaches include ad hoc physical descriptors [14–18], *N*-point correlation functions [19–22], spectrum density function [23,24], and random fields [25,26]. In recent years, deep learning models have attracted great attention in structure/microstructure design optimization. Autoencoders (AE), Variational autoencoders (VAEs), generative adversarial networks (GANs), and their variations have been applied to deterministic structure modeling and design [27–30]. On the other hand, transfer learning [31–33], AE/VAE/Vector Quantized Variational Autoencoder (VQVAE) [34–39], and GANs [40,41] have also been used to generate low-dimensional representations of stochastic structures. However, the capability of the deep generative models is limited by the data diversity in the training set. Previous deep generative models have only been applied to design deterministic (periodic) structures [27,28,42–45], or limited types of stochastic structures [34–36,40,41,46,47]. A unified design representation method for both deterministic and stochastic structures is still missing. A common practice is to determine the category of the microstructural system, deterministic or stochastic, before formulating and solving the design problem. Another practice, used for the design of stochastic microstructural systems, is to define ad hoc design variables based on prior knowledge (e.g., fiber orientation distribution for chopped fiber composites [14,15] and particle diameter distribution for Li-ion battery cathodes [16–18]). A major limitation of the aforementioned design methods is their inability to allow a unified treatment of deterministic and stochastic structures. These methods cannot be simply combined to allow the unified treatment of both design domains. Therefore, knowledge of the structure–property relationship is not usually transferrable from one type of microstructures to the other.

Therefore, the purpose of this research is to bridge the gap between the deterministic and stochastic microstructures. We established a highly diverse microstructure database that includes both deterministic and stochastic structural patterns and proposed a deep generative model-based methodology that (1) creates a unified microstructural design space that embodies both deterministic and stochastic microstructures and (2) enables generative design of microstructures with a tailorable level of stochasticity and desired properties. The remainders of this paper are organized as follows. In Section 2, an overview of proposed deep generative model-based design framework is presented. Section 3, 4, and 5 provide detailed explanations of the three components in the proposed framework. Section 3 introduces the first-of-its-kind high resolution microstructure database and the data generation methods. Section 4 introduces the property-aware deep generative model. Section 5 introduces the approach for design for structural stochasticity and properties. Section 6 are case studies. Section 7 concludes this paper.

2. Overview of the deep generative model-based design framework

As shown in Fig. 1, the proposed framework includes three major components:

(a) A highly diverse microstructure database that includes various types of stochastic and deterministic structural patterns. The methods for generating microstructure samples will also be introduced in Section 3. Mechanical properties and structural stochasticity are obtained for each microstructure sample.
(b) A property-aware deep generative model that provides a unified feature space that embodies both stochastic and deterministic structural patterns, as well as a supervised learning model (regressor) that links the latent features and the microstructure properties.
(c) A microstructure design approach for discovering and optimizing microstructures to achieve desired structural stochasticity and properties.

3. Mixed stochasticity microstructure database and data generation methods

The first contribution of this work is to establish a highly diverse, high-resolution database for deep generative model training and validation (Fig. 2). The data generation methods are also introduced in this section. Most of the existing microstructure databases only contain deterministic designs or limited types of stochastic designs, and some of them are bottlenecked in a low resolution, where the obliterated details reduce the generative ability of the deep learning model and thereby, simulation accuracy. The proposed database includes various categories of deterministic and stochastic microstructure patterns. Each microstructure image has a resolution of 128×128 pixels. The stochastic microstructural dataset consists of 20,000 samples of five categories: random fiber, random particle (circle), random ellipse, Voronoi, amorphous, and quasi-random patterns. The stochastic microstructural samples are generated using various stochastic reconstruction algorithms, including the statistical descriptor-based method [14,48,49], the space tessellation-based method [50–52], the spectrum density function (SDF)-based random field method [23,24,53], etc. The deterministic microstructural dataset includes 20,000 samples obtained from open access structure libraries [54,55] and our previous works on topology optimization [56]. In total, we have 40,000 samples, of which 90% are used for training and the remaining 10% are used for model generativity validation.

3.1. Generating stochastic microstructure samples by stochastic reconstruction

Stochastic reconstruction is a technique that generates random but statistically equivalent microstructures based on the input

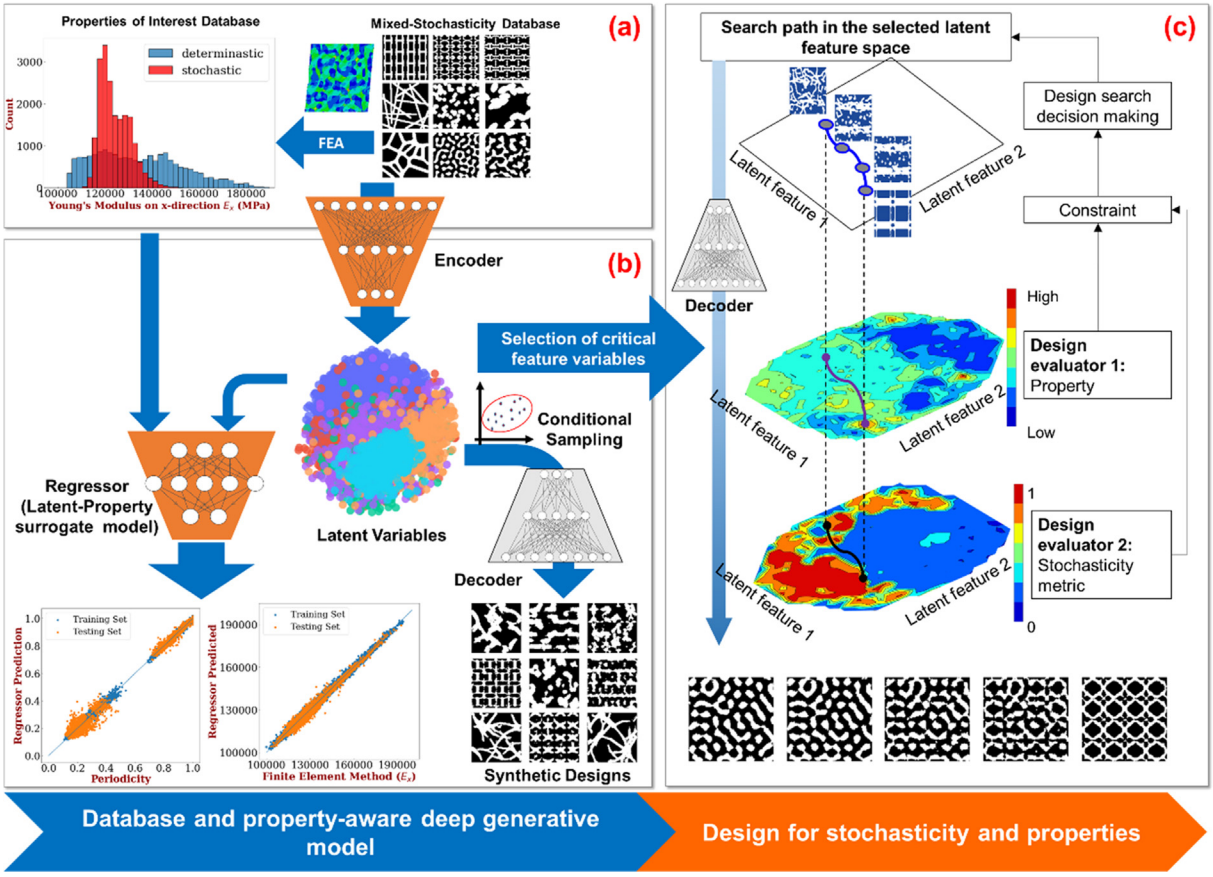

Fig. 1. The proposed deep generative model-based framework for designing microstructures for desired properties and stochasticity. (a) A highly diverse microstructure database that consists of various types of stochastic and deterministic (periodic) structural patterns. (b) A property-aware deep generative model that generates a unified feature space as the microstructure design space. (c) A design search approach that explore the unified feature space to find microstructure designs with a desired level of structural stochasticity and desired properties. The contour plots in (c) are based on the 2D t-SNE representations of the latent space, where the colors correspond to property values at different locations in the latent space.

microstructure descriptors [48,66]. For the given input microstructure statistical descriptors/functions, the stochastic reconstruction algorithm will generate random but statistically equivalent stochastic microstructure images. Stochastic reconstruction is widely used in microstructure material design [67,68], where the microstructure design is tailored by varying the input microstructure statistical descriptors/functions to achieve target properties.

This research employs three types of stochastic reconstruction algorithms to generate four categories of stochastic microstructure samples. The first is the parametric descriptor-based algorithm [14,48,51,67], which is used to generate random particle-type (spherical and ellipsoidal particles) and random fiber-type microstructures (Fig. 3). The filler centers are firstly generated randomly, then the Simulated annealing (SA) algorithm is employed to perturb particle centers to match the target distribution of dispersion descriptors (e.g., nearest neighbor distances). Lastly, the geometry of each filler is obtained by sampling on the geometry descriptor distributions (e.g., diameter, aspect ratio, orientation) until the target volume fraction is matched.

The second is the spectrum density function (SDF)-based method [23,24], which is used to generate the amorphous quasi-random microstructures with coral-like, random channel-like, or irregular connected clusters-like features. SDF is a spatial frequency function and represents spatial correlations of microstructure phases in the frequency domain. Representing a bi-phase microstructure image by function $Z(\boldsymbol{r})$ with pixel locations $\boldsymbol{r}$ and pixel values of 0 or 1, the Fourier spectrum of the microstructure image $Z(\boldsymbol{r})$ is written as:

$$\mathcal{F}\{Z(\boldsymbol{r})\} = \int_{\mathbb{R}^n} Z(\boldsymbol{r}) e^{-2\pi i \boldsymbol{r}\cdot\mathbf{k}} \mathrm{d}\mathbf{k} = A_{\mathbf{k}} \cdot e^{i\phi_{\mathbf{k}}} \tag{1}$$

where $A_{\mathbf{k}}$ and $\phi_{\mathbf{k}}$ represent the magnitude and phase information at each location $\mathbf{k}$ of the Fourier spectrum. A microstructure's SDF, $\rho(\mathbf{k})$, is defined as the squared magnitude of its Fourier transform:

$$\rho(\mathbf{k}) = |\mathcal{F}\{Z(\boldsymbol{r})\}|^2 = {A_{\mathbf{k}}}^2 \tag{2}$$

For an isotropic microstructure, the vector $\mathbf{k}$ can be reduced to its magnitude as $k = |\mathbf{k}|$; for an anisotropic microstructure, it can be defined as a function of the polar angle. Chatfield has established the mathematical connection between SDF and 2-point correlation function [69].

With an input SDF function, the corresponding stochastic microstructure image can be reconstructed using the Cahn's method. The microstructure image $Z(\boldsymbol{r})$ is represented by a Gaussian random field $Y(\boldsymbol{r})$. $Y(\boldsymbol{r})$ can be fully captured using the field-field correlation function $g(\boldsymbol{r}_1, \boldsymbol{r}_2)$. The relationships between $Y(\boldsymbol{r})$, $Z(\boldsymbol{r})$, and $g(\boldsymbol{r}_1, \boldsymbol{r}_2)$ are:

$$g(\boldsymbol{r}_1, \boldsymbol{r}_2) = \mathrm{E}[\boldsymbol{Y}(\boldsymbol{r}_1)\boldsymbol{Y}(\boldsymbol{r}_2)] = \int_0^\infty \frac{J_{(n-2)/2}(k\Delta r)}{(k\Delta r)^{(n-2)/2}} \cdot k^{n-1} \cdot \rho(k) dk \tag{3}$$

$$\Delta r = |\boldsymbol{r}_1 - \boldsymbol{r}_2| \tag{4}$$

$$Z(\boldsymbol{r}) = \begin{cases} 1, & Y(\boldsymbol{r}) \le \alpha \\ 0, & Y(\boldsymbol{r}) > \alpha \end{cases} \tag{5}$$

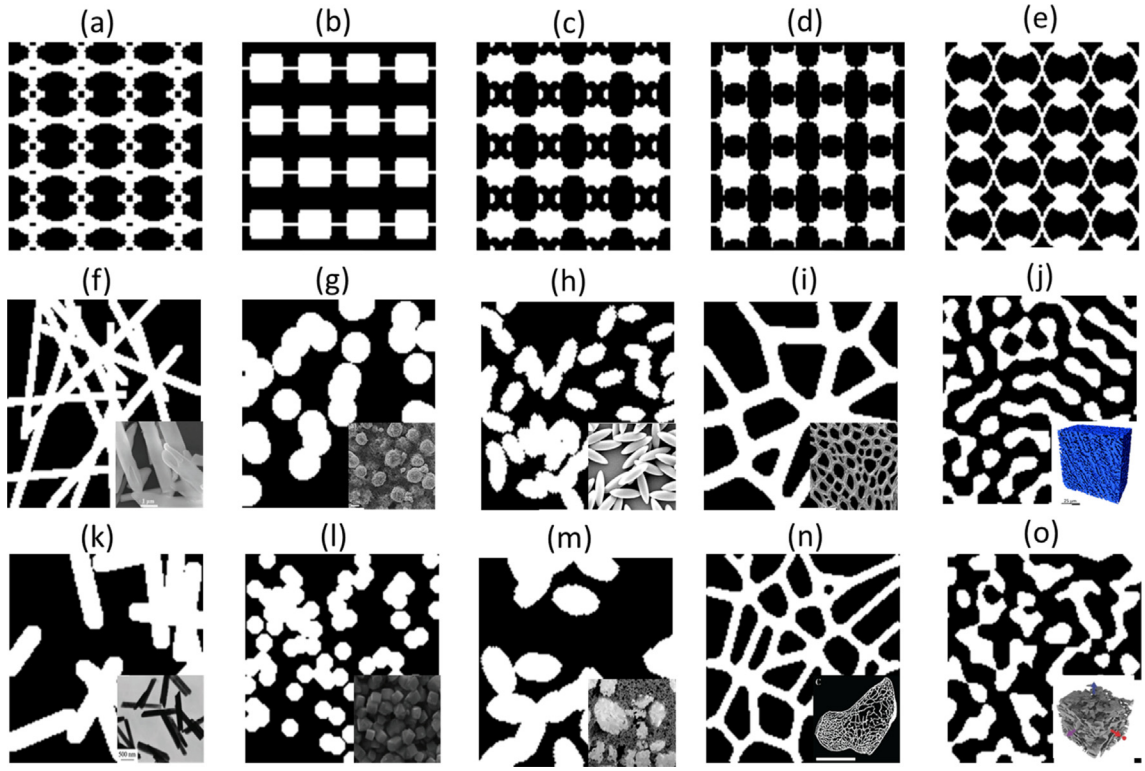

Fig. 2. Examples of deterministic (periodic) and stochastic microstructure samples in the database: (a)∼(e) are deterministic microstructure samples. (k)∼(o) are stochastic microstructure samples and real microstructures images showing similar features. (f) A random fiber microstructure and an FESEM image of $NaYF_4$ using NaF as fluoride source at pH = 3. Reproduced with permission. [57] Copyright 2015, Elsevier. (g) A random particle microstructure and a SEM image of a commercial NMC cathode. Reproduced with permission. [58] Copyright 2019, Elsevier. (h) A random ellipse microstructure and a SEM image of the Pennsylvania Green Polystyrene (PS-PG) ellipsoids. Reproduced with permission. [59] Copyright 2021, American Physical Society. (i) A random cellular microstructure and a microphotograph of green tissue-microstructure in Eucalyptus globulus. [60] (j) A quasi-random microstructure and a 3D rendering of electrode microstructures made by IIT. Reproduced with permission. [2] Copyright 2018, Wiley. (k) a random fiber microstructure and a TEM image of β-$NaYF_4$: Yb^{3+}, Er^{3+} nanocrystals synthesized with 1.25 g NaOH. Reproduced with permission. [61] Copyright 2017, Elsevier. (l) A random particle microstructure and a FESEM image of $BaYF_5$ with RE^{3+}/EDTA. Reproduced with permission [62]. Copyright 2011, Royal Society of Chemistry. (m) A random ellipse microstructure and a SEM image showing the CBD morphology alongside the secondary NMC particles [63]. (n) A random porous microstructure and a microscopic image of a bone [64]. (o) An amorphous microstructure and a SEM image of NMC particles. Reproduced with permission. [65] Copyright 2014, Wiley. (For interpretation of the references to colour in this figure legend, the reader is referred to the web version of this article.)

where $\rho(\boldsymbol{k})$ is the SDF. J are Bessel functions. A numerical realization of the GRF for a targeting SDF is constructed using the wave-form method [70]:

$$Y(r) = \sqrt{\frac{2}{N}} \cdot \sum_{i=1}^{N} \cos(k_i \boldsymbol{k}_i \cdot \boldsymbol{r} + \phi_i) \tag{6}$$

where N is the number of terms in the truncated series, ϕ_i is generated by sampling uniform distribution in the range of [0, 2 π], $\boldsymbol{k_i}$ is a vector uniformly distributed on a unit sphere, and k_i is a scalar obtained by sampling the probability density function $\rho(\boldsymbol{k}) \cdot \boldsymbol{k}$ in the range of $(0, \infty)$. A realization of the GRF $Y(\boldsymbol{r})$ is a pixelated greyscale image, and the corresponding binary microstructure image can be obtained by setting a greyscale threshold. By changing the input spectrum density function $\rho(\boldsymbol{k})$, a variety of microstructure patterns can be obtained from Fig. 3(c).

The third is the stochastic Voronoi tessellation-based method, which is used to generate stochastic cellular-type and network-type microstructures (Fig. 3(b)). Similar to the descriptor-based algorithm, this algorithm starts from generating and perturbing the Voronoi cell centers in a 2D square domain. With a distance metric, e.g., Euclidean distance or Manhattan distance, the midpoint of the shortest distance for the nearest pair of cell centers is calculated, where the isometric perpendicular line is drawn as the cell boundary. The white pixels are added along the cell boundaries until the target volume fraction is reached. By varying the input statistics, various microstructural images can be obtained. A total of 20,000 stochastic microstructures are included in the dataset to keep the balance between stochastic and deterministic samples.

3.2. Generating deterministic (periodic) microstructure samples

The deterministic microstructure samples are either obtained from open access metamaterial structure libraries [54,55] or generated in our previous works on topology optimization [56]. The optimal number of structural units in an image is determined by matching the spatial correlation length of the structural characteristics with those of the stochastic structure images. 20,000 deterministic structure images in each 2 × 2, 4 × 4, 6 × 6, and 8 × 8 unit arrangement are tested to find the optimal number of units (Fig. 4). The test criterion is to match the average spatial correlation length of the structural characteristics observed in the stochastic structure image samples (20000 samples in total). From the signal processing point of view, a similar spatial correlation length indicates a similar frequency of the signal. The spatial correlation length is evaluated using the 2-point correlation function [71,72], which is defined as:

$$\boldsymbol{S}_2^j(\boldsymbol{r}_1, \boldsymbol{r}_2) = \left\langle I^j(\boldsymbol{r}_1), I^j(\boldsymbol{r}_2) \right\rangle \tag{7}$$

where I is an indicator function at location $\boldsymbol{r}$ in the space:

$$I^j(\boldsymbol{r}) = \begin{cases} 1, when r is in phase j \\ 0, otherwise. \end{cases} \tag{8}$$

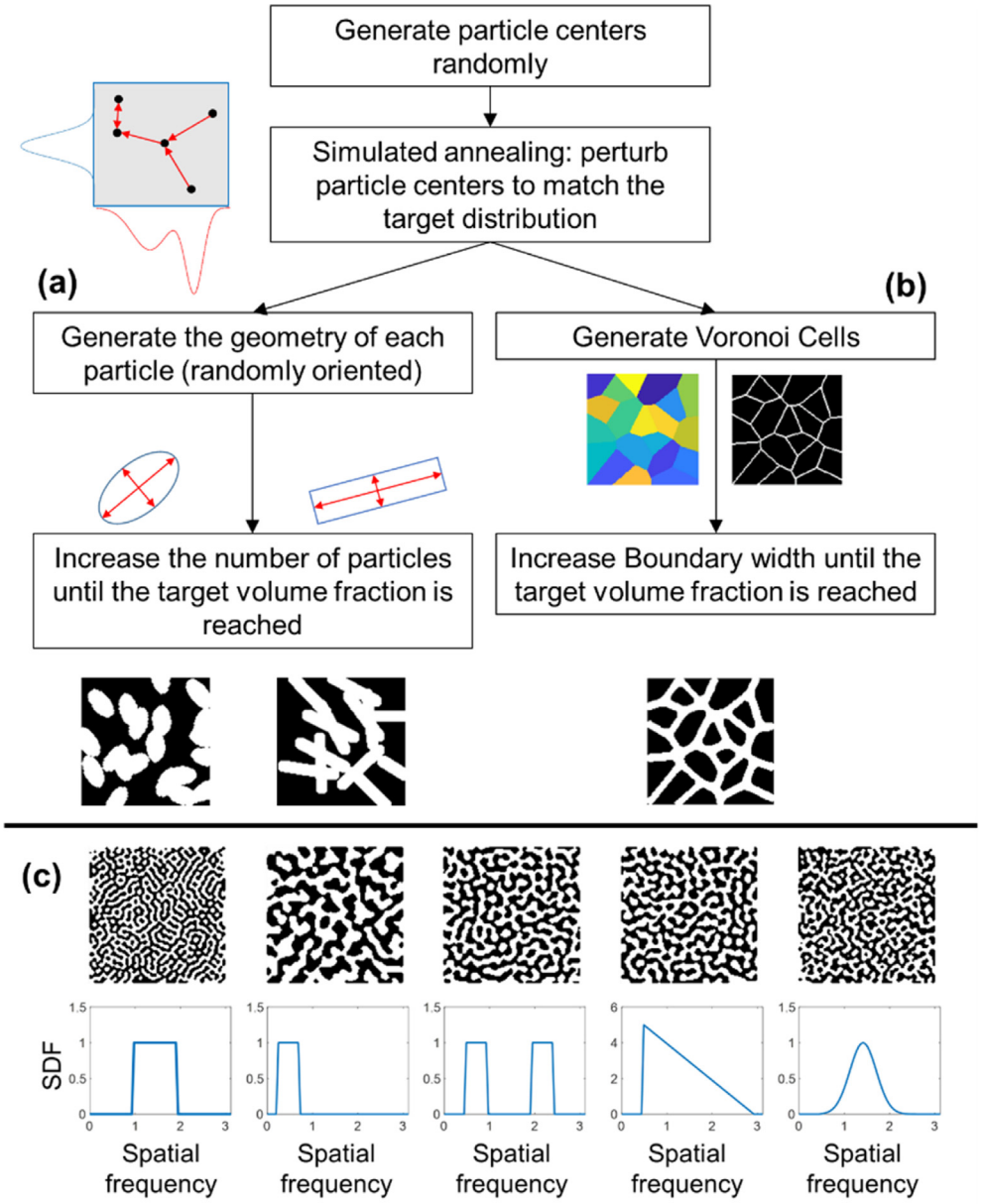

Fig. 3. (a) Statistical microstructure parameter-based reconstruction, and (b) Stochastic Voronoi tessellation-based reconstruction, and (c) Generation of various microstructure samples by varying the input spectrum density function.

Here we focus on the short-distance correlations (e.g., the 2-point correlation value when the distance in pixel is in the range of [0, 10]), which have a higher impact on the structure morphology than the long-distance correlations. Obviously, deterministic images with 4 × 4 structural units have the closest match to the stochastic structure images.

3.3. Creating the grayscale master image of each microstructure sample by Euclidean distance transform

The binary microstructure image samples obtained from open access data sources always have a pre-determined volume fraction, which is the ratio between white pixels and the total number of pixels in our case. To provide the flexibility to generate microstructure samples with a wide range of volume fractions, we create a "greyscale master image" by blurring an original binary sample image using Euclidean distance transform. For each white/black pixel in the binary image, we evaluate the Euclidean distance from this pixel to the nearest boundary. The normalized distance values are used as the greyscale value of this pixel. By varying the greyscale threshold for binarization, binary microstructure images of different volume fraction values can be generated based on the corresponding greyscale master image.

In Fig. 5, we show a few examples of the greyscale master images and the binary microstructure images generated with different volume fractions. It is recommended to use a volume fraction range of [pre-determined volume fraction ± 0.25] in order to maintain the morphological features, based on our observation. In this work, we use a volume fraction of 40% for all samples in order to focus on the effect of structural stochasticity on microstructure properties.

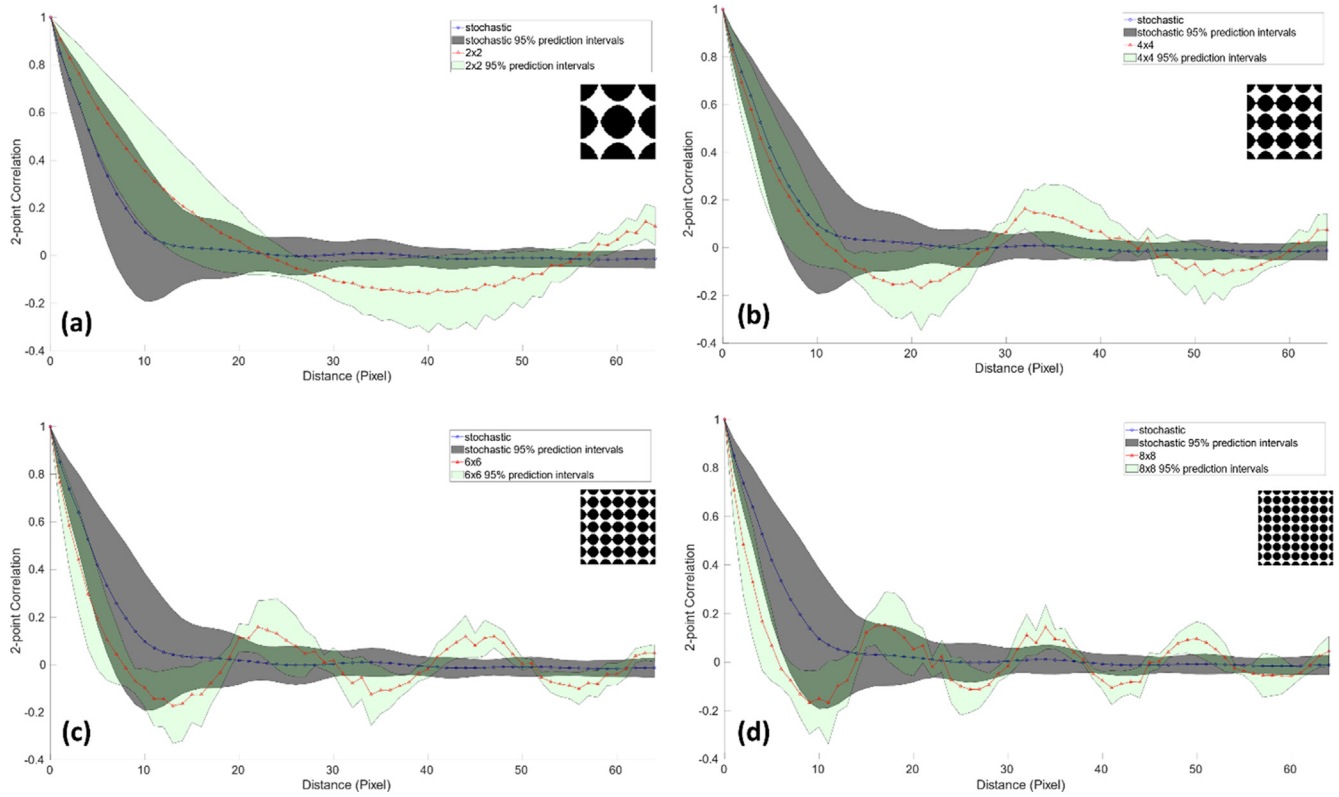

Fig. 4. Statistics of the 2-point correlation functions for stochastic and deterministic (periodic) microstructures with different arangements of (a) 2×2, (b) 4×4, (c) 6×6, (d) 8×8 structural units. The mean and 95% prediction intervals of the 2-point correlation functions are obtained based on all 20,000 deterministic/stochastic samples. Only one microstructure sample is shown in each plot for illustrative purpose.

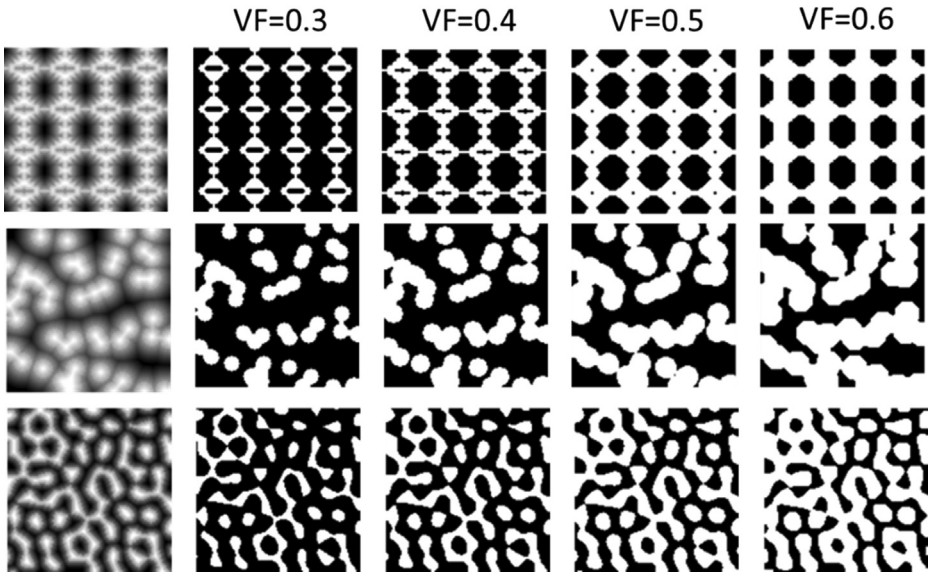

Fig. 5. Greyscale images created by Euclidean distance and the binary image with volume fraction of 0.3, 0.4, 0.5, and 0.6.

3.4. Evaluation of microstructure sample properties: Structural stochasticity and mechanical properties

A quantitative measurement of the "stochasticity level" is indispensable for describing and tailoring stochastic microstructural characteristics. We propose a new stochasticity metric based on spectrum analysis, which is widely employed in analyzing the frequency/stochasticity of 2D images. According to the Wiener-Khinchin Theorem [73], the autocorrelation function $\mathbf{C}(t)$ of a 2D image is expressed as

$$\boldsymbol{C}(t) = F^{-1}\left[\bar{\boldsymbol{H}}(\omega)\boldsymbol{H}(\omega)\right] = \frac{1}{2\pi}\int_{-\infty}^{\infty}\bar{\boldsymbol{H}}(\omega)\boldsymbol{H}(\omega)e^{i\omega t}d\omega \tag{9}$$

where the$H(\omega)$ denotes the Fourier transform of the 2D image $\boldsymbol{h}(t)$ in the form of

$$\boldsymbol{H}(\omega) = F[\boldsymbol{h}(t)] = \int_{-\infty}^{\infty} \boldsymbol{h}(t) e^{-i\omega t} dt \tag{10}$$

and $\bar{\boldsymbol{H}}(\omega)$ denotes the complex conjugate of the Fourier transform. In a binary 2D image $\boldsymbol{h}(t)$, the phase with higher volume fraction is marked by 0 and the other phase is marked by 1 when calculating the autocorrelation.

For a two-phase image, the maximum value of its autocorrelation function is equal to the volume fraction. The autocorrelation function can be normalized by min–max scaling into the range of [0,1] for a fair comparison among microstructure samples with different levels of volume fractions. The normalized autocorrelation function $\mathbf{C}(t)$ of a periodic image has multiple periodic local maxima at 1 and local minima at 0. By contrast, the autocorrelation function of a stochastic image has random oscillations with a higher frequency and a smaller magnitude. The 3D view of autocorrelation function for a transition in microstructural patterns are shown in Fig. 6(b).

The range between maxima and minima of the normalized autocorrelation function works as an indicator of the structural stochasticity. Let $\{m_1, m_2, \cdots, m_n\}$ be a sequence that contains all local maxima of the normalized autocorrelation function $\mathbf{C}(t)$, where the m_1 is the global maximum that is always equal to 1, and m_2 is the second highest local maximum. The global minimum is always equal to 0 after normalization. Then the proposed metric P is defined as:

$$P = m_2 \tag{11}$$

Based on our test presented in Fig. 6(a), we observe that the proposed metric P provides a continuous measurement of the structural stochasticity. When $P = 1$, the image has a perfectly periodic structural pattern. When $P = 0$, the image is a white noise signal. When $P > 0.5$, a clear periodic pattern can be observed in the image. To demonstrate the proposed stochasticity metric is consistent for a wide range of volume fraction values, we binarize greyscale master images with different levels of volume fraction and evaluate the metric value for each binary image. The results demonstrate that the volume fraction has a low impact on the stochasticity metric value. The results are shown in Fig. S4 in the Supporting Information.

For the mechanical properties, we choose elasticity as an example to test the proposed property-driven microstructure design approach. A finite element model (FEM) with unified periodical boundary conditions [74] is established to simulate the homogenized stiffness properties for each microstructure, including Young's moduli in the x-direction and y-direction (E_x, E_y), shear modulus (G), and Poisson's ratio (ν). The microstructure has two phases assigned with different material properties. The elastic modulus and Poisson's ratio of the white phase in the microstructure are $E_{Boron} = 379300\,\text{MPa}$ and $\gamma_{\text{Boron}} = 0.1$, whereas $E_{\text{Aluminum}} = 68300\,\text{MPa}$, $\gamma_{\text{Aluminum}} = 0.3$ for the black phase. The homogenized stiffness properties can be obtained by Eqs. (A1)–(A3) from the FEM simulation results, and more details regarding the simulations can be found in the Appendix.

4. Property-aware deep generative modeling: unified feature space representation and microstructure-property prediction

The key idea is to learn a unified feature space representation of the stochastic and deterministic microstructure patterns as the design space, and then to establish the relationship between the feature variables (microstructure design variables) and the properties of interest to enable the property-driven microstructure design. Three deep generative models, AE, VAE, and Adversarial Autoencoder (AAE) are compared to understand their relative merits. Furthermore, we compare the proposed property-aware deep generative modeling strategy with the widely used separate modeling strategy, where the deep generative model and the regressor are trained independently.

4.1. Comparison of three deep generative models for feature learning

The AE is a widely used deep neural network architecture that essentially performs dimensionality reduction. An autoencoder is a combination of two neural networks, (1) an encoder that maps input data into a low-dimensional latent space and (2) a decoder that reconstructs the corresponding input based on a latent feature vector. Experimentally, we have discovered that the encoder from AE can capture the visual features and topology relations, and then reconstruct input training images accurately. However, the model will result in poor generality due to the unregularized latent space, and the decoder cannot generate new designs based on latent samples drawn from any probability distributions. Moreover, the similarity of structural features cannot be measured by the distance in the latent space. For example, the intermediate point between two deterministic microstructure samples in the latent space might be decoded to a stochastic microstructure that does not resemble the

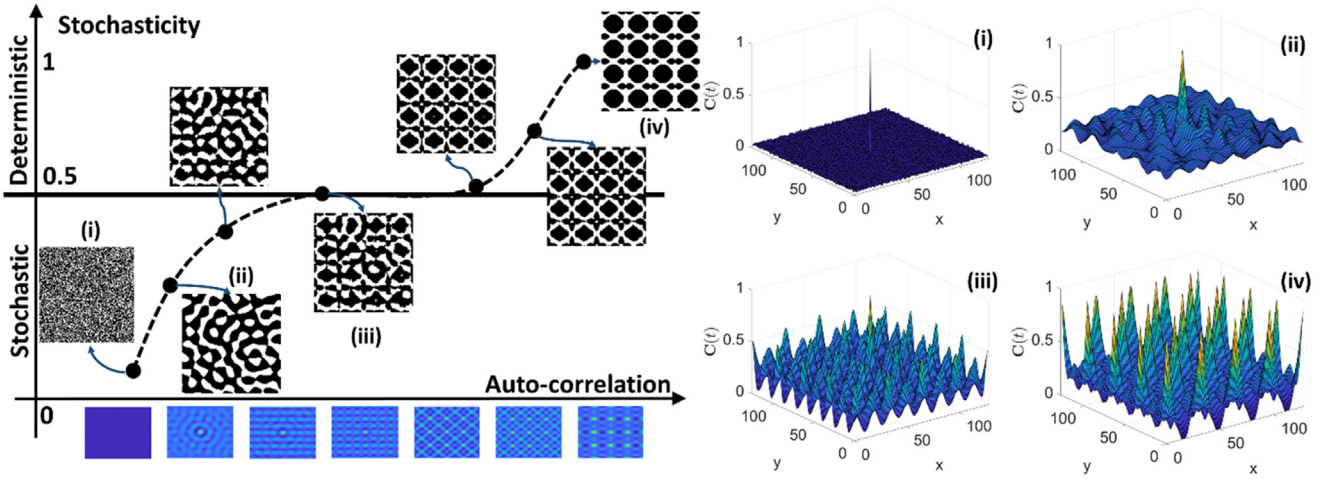

Fig. 6. A Fourier spectrum-based metric for quantifying the structural stochasticity. (a) Continuous transition in microstructural pattern and the corresponding stochasticity metric values. Sample (i) is a binary white noise image. The 2D views of the seven samples' autocorrelation functions are shown under the horizontal axis. (b) The 3D views of autocorrelation functions of samples (i)∼(iv).

two original designs, which is shown in Fig. A1 in the Appendix. Therefore, AE does not provide the capability of morphing microstructure designs continuously to achieve desired stochasticity/morphological characteristics. To overcome the issue of lack of generality, VAE, GAN, and their variants, such as AAE, Conditional Generative Adversarial Network (cGAN), and Wasserstein Generative Adversarial Network (WGAN), have been employed in generative design. However, GAN models suffer from diminished gradient, model collapse, and other training instability issues that limit their potential to be used as general models for complex problems [75,76]. Considering the high complexity of microstructural characteristics and the great diversity of microstructural patterns, we propose to establish property-aware deep generative models based on VAE and AAE in this work.

Similar to the autoencoder, VAE models contain an encoder and a decoder, but in VAE models, the latent space $\boldsymbol{Z}$ is regularized towards a prior distribution such as Gaussian and Gaussian-mixture. In the proposed VAE architecture (Fig. 7(c)), the encoder has 4 blocks starting with convolutional layer and ending with a max-pooling layer, and two fully connected layers (FC layers) following the last block compressing the features into two 100-dimensional latent vectors that denote the mean and variance. The architecture of the decoder uses fully connected layers with fewer neurons to avoid overfitting, and the other layers are almost

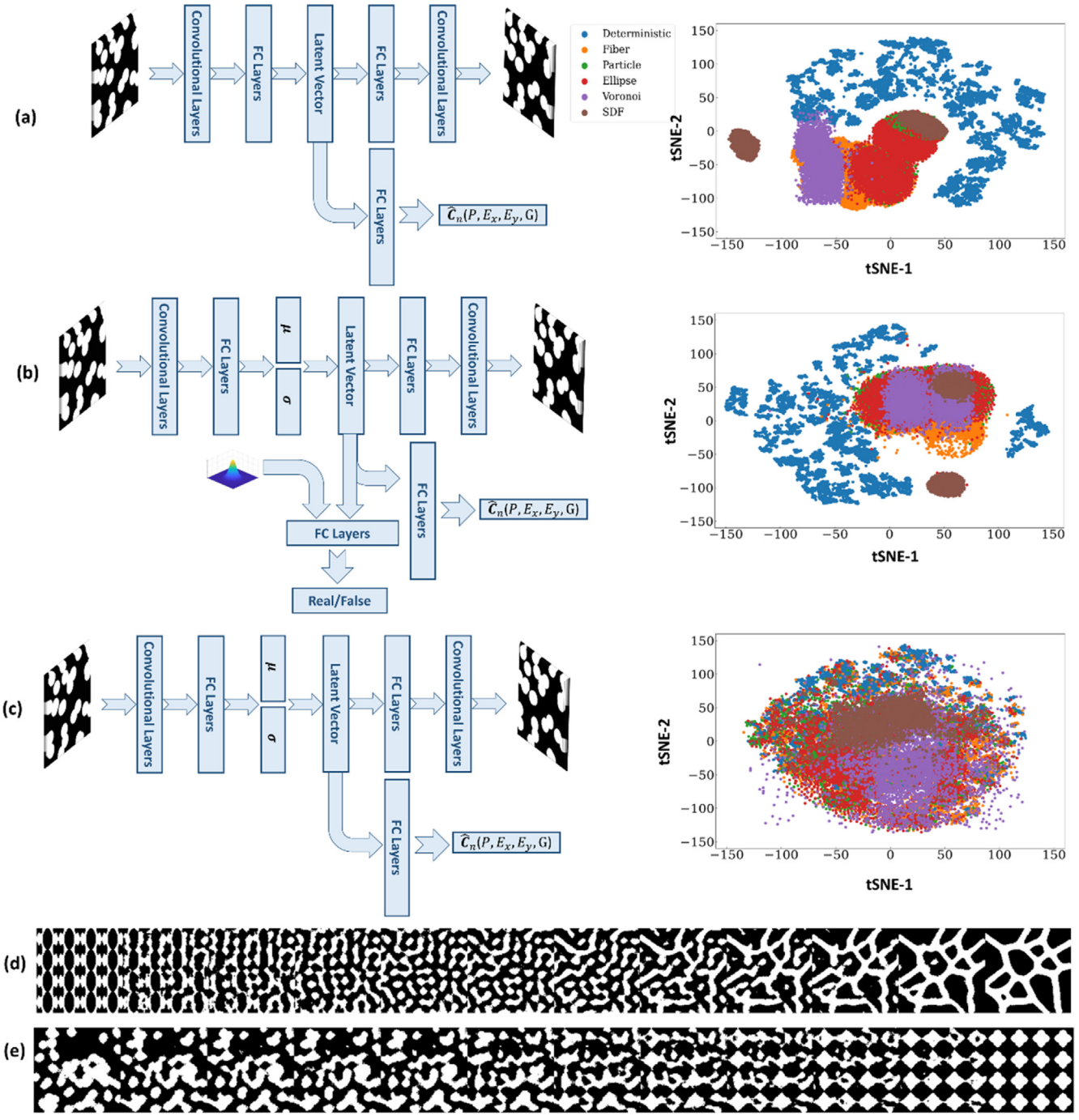

Fig. 7. Architecture and two component T-SNE visualization of the latent feature space for (a) AE (b) the AAE model, (c) VAE. (d) and (e) show the continuous transition between two microstructure designs by conducting linear interpolation between two design points in the latent space. "FC layer" stands for fully connected layer.

symmetrical with the encoder. A general loss function of VAE is expressed as

$$L_i(\theta,\phi) = -E_{z\ q_\theta(z|x_i)}\left[log p_\phi(x_i|z)\right] + D_{KL}(q_\theta(z|x_i)|p(z)) \quad (12)$$

where x_i is input data, z is the latent vector, and θ, ϕ denote the parameters of the decoder and encoder respectively. The first term is the reconstruction loss that measures the pixel-level error between the input and reconstruction, where the mean square error (MSE) is employed commonly for computer vision tasks. The second term, denoting the KL loss, is calculated from the sum of the Kullback-Leibler Divergence, which ensures that the learned distribution q follows the true prior distribution p. Including the KL term in the loss function can regularize the latent space and reduce discontinuities between latent vector clusters. The standard loss function formulation in Eq. (12) works well in capturing deterministic microstructural patterns [54,77,78], while literature [35,40,79] and our experiments suggest that the style loss significantly improves the reconstruction quality for the stochastic microstructures, and, therefore, reduces the latent vector dimensions. Style loss represents the correlation between feature maps and was initially introduced for texture synthesis. The style loss is defined as

$$L_{STYLE} = \sum_l \sum_{i,j} \left(G^l_{i,j} - A^l_{i,j}\right)^2 \quad (l = 1,2,3,4) \quad (13)$$

where $G^l_{i,j}$ and $A^l_{i,j}$ are the Gram-matrix of reconstructed images and input images. The gram-matrix is obtained by

$$G^l_{ij} = \sum_k F^l_{ij} F^l_{ij} \quad (14)$$

where F^l_{ij} is the feature map that is usually extracted from the l th convolutional layer of a pre-trained VGG-19 model [79–81]. Note that l is selected as 1,2,3,4 empirically, which is the first convolution layer at the 1st ∼ 4th "block" of VGG-19.

The latent vectors extracted by the stand-alone VAE may only contain information describing the geometries of microstructures [54]. To improve the accuracy of predicting the structure–property relationship, we propose a property-aware deep generative model by attaching a regressor to the VAE model. The regressor is trained simultaneously with the encoder and decoder to predict the relationship between the latent variables (microstructure design variables) and the microstructure properties C_n, e.g., the stochasticity (P) computed by Eq. (11) and the elastic constants (E_x, E_y, G). In this way, the knowledge of microstructure properties is embedded in the learned latent space. The regressor loss defined as

$$L_{REGRESSOR} = \frac{1}{n}\|C_n - \hat{C}_n(z)\| \quad (15)$$

is added to the VAE loss, where $\hat{C}_n$ is the predicted microstructure properties. Therefore, the proposed loss function for the property-aware deep generative model is written as:

$$L_{total} = L_{RECONSTRUCTION} + L_{KL} + L_{STYLE} + L_{REGRESSOR} \quad (16)$$

Besides VAE, another option is to use AAE to construct the proposed property-aware deep generative model. AAE [82] is an adversarial model that uses a similar idea to VAE but introduces additional regularization to the latent vectors with a discriminator. The general loss function of AAE is defined as

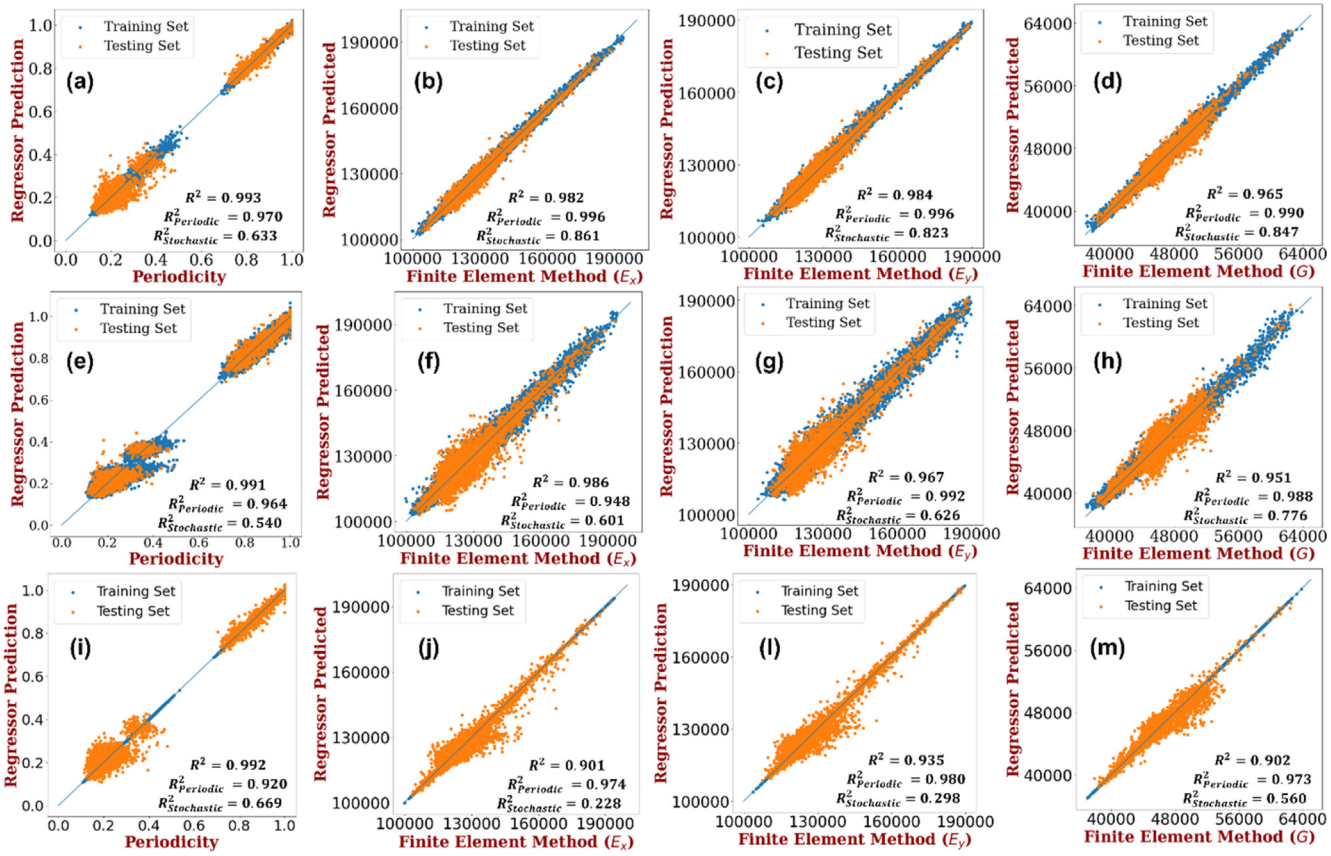

Fig. 8. Comparison of the property prediction accuracies of different modeling strategies. (a)∼(d) Regressor in the property-aware deep generative model. (e)∼(h) The stand alone DNN regressor trained independently from the deep feature learning. (i)∼(m) The stand alone GPR regressor trained independently from the deep feature learning. The R^2 values on all data in the test set, only the deterministic (periodic) samples in the test set, and only the stochastic samples in the test set are provided in each subplot.

$$L_{AAE} = E_{\boldsymbol{x}}\left[E_{\boldsymbol{q}(\boldsymbol{z}|\boldsymbol{x})}[-log\boldsymbol{p}(\boldsymbol{x}|\boldsymbol{z})]\right] - E_{\boldsymbol{x}}\left[\sum_i log\boldsymbol{\sigma}_i(\boldsymbol{x})\right] + E_{\boldsymbol{q}(\boldsymbol{z})}[-log\boldsymbol{p}(\boldsymbol{z})]$$

$$= L_{RECONSTRUCTION} - Entropy + CrossEntropy(\boldsymbol{q}(\boldsymbol{z}), \boldsymbol{p}(\boldsymbol{z})), \quad (17)$$

where we add the style loss term similar to VAE and use a gaussian prior.

The latent feature space is visualized using the t-distributed stochastic neighbor embedding (t-SNE) [83] method. t-SNE is a nonlinear dimensionality reduction method that compresses data into a visualizable lower dimensional space, usually, 2 or 3 dimensions. This method minimizes the Kullback-Leibler divergence between the joint probabilities of high dimensional and low dimensional data. We visualize the t-SNE space for AE, VAE, and AAE, as shown in Fig. 7. The major issue with AE is that different categories of microstructure samples are widely separated in the t-SNE space. It indicates that abrupt changes in microstructure characteristics will be observed when moving the point in the original latent feature space, which is not desirable for continuous microstructure morphing. AAE achieves the same level of reconstruction quality as VAE, while it has a similar issue as AE that different category of microstructure samples are separated by huge gaps in the t-SNE space. Therefore, we select the VAE model in the rest of the study. The model architecture is determined empirically and tuned based on the reconstruction quality and the regression accuracy. The model specifications are provided in Table S1 in the Supporting Information. We decide to use a 100-dimensional latent vector in order to keep a balance between the reconstruction quality and the optimization efficiency. We also established a larger synthetic database by decoding latent vector sampling from the prior distribution, which can fulfill the need to impove regressor accuracy and train larger generative models in the future. The latent space provides the capability of morphing one microstructure design to another in a continuous manner. A continuous path in the latent feature space can be decoded to obtain a continuously morphing microstructure series. Two examples of the continuous transition between a stochastic microstructure and a deterministic structure obtained by the latent space are demonstrated in Fig. 7(d) and (e). More examples of generating new microstructure patterns by sampling the latent space are shown in Fig. S1 in the Supporting Information.

4.2. Comparison of the property-aware modeling strategy and the separate modeling strategy

Here we compare two modeling strategies: (i) the property-aware deep generative modeling strategy that trains the VAE and the regressor simultaneously, and (ii) the separate modeling strategy, which trains the VAE firstly to obtain the latent feature space and then trains the regressor to link the latent features to the properties of interest. For the separate modeling strategy, two widely used supervised learning models, Gaussian process regression (GPR) and deep neural network (DNN), are tested. As shown in Fig. 8, the property-aware generative model achieves the highest regression accuracy in both stochastic and deterministic microstructures. By contrast, the separating modeling strategy has difficulties in predicting the mechanical properties of the stochastic samples. The R^2 values on the test set could be as low as 0.228 when predicting E_x of the stochastic samples. Despite the low accuracy in these test cases, we acknowledge the convenience of the separate modeling strategy. With a pretrained latent feature space, the designers can easily link it to any material properties of interest by design-of-experiment and surrogate modeling, without retraining the deep generative model. But in this work, we select the property-aware modeling strategy for its higher accuracy.

5. Design for structural stochasticity and properties

Structure design optimization in a high dimensional space requires a large number of design evaluations (simulations) in each iteration to obtain either the numerical gradient used in gradient-based optimization methods [84,85] or the fitness values of all newly generated designs for evolutionary optimization methods [86–88]. Considering the cumulative computational cost of design evaluations, the regressor introduced in Section 4.1 is used to replace the high-cost simulations in design search.

New microstructure designs can be generated by conducting arithmetic operations on the latent feature variables. Properties of the new designs will be evaluated by the regressor, and the stochasticity will be evaluated using the stochasticity metrics discussed in Section 3.4. As structural stochasticity can be linked to the selection and control of manufacturing processes [89,90], the proposed stochasticity tailoring method is conducive for introducing manufacturing capability as the design constraints.

A new generative design approach is proposed to generate microstructure designs with (1) continuous transition in structural stochasticity and (2) target properties. The authors propose to formulate it as a path-planning problem in the latent feature space. Starting from the original design, the design goal is to find a transition path σ^* in the latent feature space that leads to the desired properties while satisfying requirements on the searching path, such as monotonously increasing/decreasing structural stochasticity.

Gradient-based optimization methods, e.g., gradient descent, can discover the steepest path in minimizing or maximizing the stochasticity, however, the explicit analytic gradient expression is not available, and the numerical gradient may lead the optimizer to saddle points or local optima. Evolutionary optimization algorithms, e.g., Genetic Algorithm [91,92] and Non-dominated Sorting Genetic Algorithm-II (NSGA-II) [93], suffer less from the local minima issue and have more flexibility in setting multi-objective, bounds, and non-penalty constraint, thereby allowing us more degree of freedom in searching multiple selected properties in the desired stochasticity range. In the following case studies, we use the latent vector $\mathbf{z}$ of an existing design as the starting point to search for the optimal design or the Pareto Frontier under multiple design objectives. In each generation, the two objective function values are normalized by the ideal and nadir point, and the best design is selected firstly by the rank (non-dominated sorting) and finally by crowding distance sorting (Manhattan distance). The major program of the algorithm is implemented with PyTorch and the Python module pymoo [94] and will be available by request.

One application of the proposed design framework is to discover new deterministic microstructures (e.g., periodic metamaterial design) with equivalent or better performances based on a known stochastic microstructure exemplar, or vice versa. We consider it as a process of increasing/decreasing the structural stochasticity while maintaining/improving the properties. To further reduce the dimensionality of the design space, feature selection is conducted to identify latent features that control the structural stochasticity while having minimal/significant influence on microstructure properties. ReliefF and RReliefF [95–98] are employed to rank the latent features based on their contribution to the structural stochasticity and properties. To find a stochastic/deterministic microstructure design with equivalent properties of an exemplar, it is formulated as a single objective optimization problem:

$\min/\max P(\mathbf{z})$ if searching for a stochastic design/a deterministic design

Subject to:

$$g(\boldsymbol{z}) := |\widehat{C}_0(\boldsymbol{z}) - \widehat{C}_0(\boldsymbol{z}_0)| < \\ < \tau_0 to maintain a property from starting point,$$

$$\boldsymbol{z} \in \boldsymbol{Z}$$

where $\mathbf{z}_0$ is the start latent vector of the search path, which was encoded from the original design. $\boldsymbol{Z}$ indicate the latent feature space, and τ_0 is the tolerance for the property constraint.

To find a stochastic/deterministic microstructure design with optimal properties, it is formulated as a multiple objective optimization problem:

$$\min/\max \begin{cases} P(\boldsymbol{z}) if searching for a stochastic design / deterministic design \\ \widehat{C}_1(\boldsymbol{z}) if searching for control one \end{cases}$$

Subject to:

$$g(\boldsymbol{z}) := |\widehat{C}_0(\boldsymbol{z}) - \widehat{C}_0(\boldsymbol{z}_0)| < \tau_0 to maintain a property from starting point,$$

$$f(\boldsymbol{z}) := |\widehat{C}_2(\boldsymbol{z}) - \widehat{C}_3(\boldsymbol{z})| \\ < \tau_{23} to maintain difference between two properties,$$

where τ_{23} is the tolerance for the constraint between two comparative properties $\widehat{C}_2$ and $\widehat{C}_3$.

6. Design cases and validation

Three design cases presented in this section demonstrate the effectiveness of the proposed design methodology. Case 1 is to demonstrate the microstructure methodology on single-objective design problems, where we search for deterministic/stochastic microstructures that possess equivalent properties as the initial design that is stochastic/deterministic. In addition to the cases presented in this section, more test cases can be found in Fig. S3 in the Supporting Information.

In Case 1 (a), we start from a random network-like stochastic microstructure to generate a series of microstructure designs with monotonic decreasing stochasticity while maintaining Young's modulus along x-direction E_x with a tolerance of ± 3% (132127 ± 3964 MPa). The final design is a deterministic pattern, which is considered as a metamaterial design inspired by the stochastic microstructure. In Case 1 (b), we start the search from a deterministic microstructure pattern and our goal is to generate a series of microstructures with equivalent E_x with a tolerance of ± 3% (126450 ± 3794 MPa). and monotonic increasing structural stochasticity. The final design is a random irregular particle-like microstructure [99] that resembles the particle reinforced metal composites, which is considered as a low-cost substitute for the original deterministic metamaterial design that requires multimaterial additive manufacturing. The obtained design series are shown in Fig. 9(a) and (b).

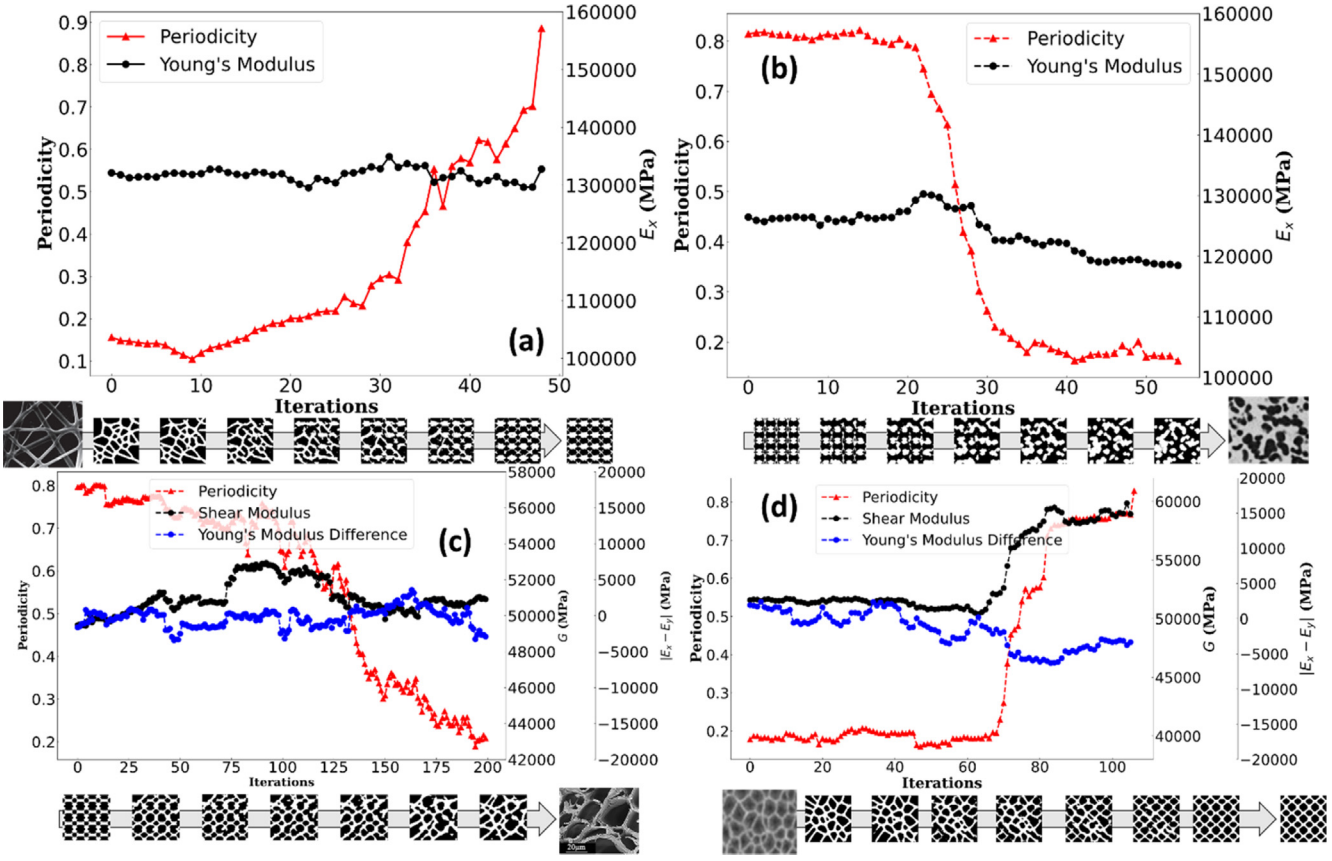

Fig. 9. Design cases on microstructure design. (a) Search a deterministic (periodic) microstructure with equivalent Young's modulus from a nano fibrous web-like microstructure [101]. Reproduced with permission, Copyright 2013, SAGE Publications. (b) Search a stochastic microstructure with equivalent shear modulus as the start point, a deterministic design. SEM photo adapted from Emamian (2011) [99]. (c) Search a stochastic microstructure with maximum shear modulus and equivalent Young's modulus in both x- and y-direction. SEM photo adapted from Wu (2021) [102]. (d) Search a deterministic microstructure with maximum shear modulus and equivalent Young's modulus in both x-direction and y-direction from a porous-silicon-like microstructure [103]. Copyright 2016, Elsevier. It is to be noted that the material property data shown in this figure are true properties (confirmed by simulations). During the design process, the regressor-predicted properties are used to guide the optimal search. The optimization history plots using regressor-predicted properties are shown in Fig. S5 in the Supporting Information.

Case 2 is to evaluate the proposed method on multi-objective design problems. The two design objectives are to minimize the structural stochasticity, meanwhile, maximize the shear modulus. We also impose the constraint of equivalent Young's modulus along x- and y-direction on the design, where the tolerance is defined as $|E_x - E_y| < 5,000MPa(5\%)$. The design search starts from a deterministic microstructure pattern. The proposed method generates a series of designs with decreasing structural stochasticity and increasing shear modulus. As shown in Fig. 9(c), one interesting finding is that the proposed method evolves the microstructure design into a stochastic pattern that resembles the microstructure of natural wood [100]. This indicates that our method successfully finds a natural microstructure as the substitute for the deterministic engineering pattern. We also demonstrate a successful multi-objective search along the stochastic-to-deterministic direction with the same objective functions and constraint, which is shown in Fig. 9(d). A stochastic foam-like microstructure is evolved into a deterministic structure pattern by the proposed method.

In Case 3, we use the "microstructure building blocks" obtained in the Case 1 (b) to construct stochastically graded structures. Case 3 demonstrates the potential of manipulating stress wave propagation behaviors by varying the local microstructural stochasticity, while maintaining the stiffness and weight of the structure. A series of nine "microstructure building blocks" with continuously increasing stochasticity and the same elastic modulus are generated and assembled into a beam structure. The total length of the beam is 1000 mm. All the building blocks have the same composition, composition fractions and stiffness, thus the weight and stiffness of the beam structure is invariant regardless which building blocks are used. Three beam structure designs are compared: (i) a structure with stochastic microstructure blocks only, (ii) a structure with deterministic microstructure blocks only, and (iii) a stochastically graded structure with a continuous transition from deterministic to stochastic to deterministic, as shown in Fig. 10 (a). More stochastically graded structure designs are tested and compared in Fig. A3 and Fig. S6. The impact simulations are implemented in LS-DYNA with single precision explicit analysis. The two material phases are the same as what we use in section 3.4. Detailed information on material properties used in the simulation is provided in Table S2 and Fig. S2 in the Supporting Information. An impact load with an initial force of 10kN is applied to the right end of the structure, of which the left end is attached to a fixed rigid plate. Here we investigate the influence of structural stochasticity on the stress wave propagation in the structure. The effective stress distributions inside each structure when time = 0.485 ms are shown in Fig. 10(b). The stress wave propagation behavior is captured by the plot of time-distance-maximum effective stress, as shown in Fig. 10(c). Fig. 10(d) shows the maximum effective stress versus time observed at 800 mm from the impact end in the structure. The stress wave propagation speed is measured by the time when the observation location reaching the peak of the effective stress. In this test case, the stress wave propagates the fastest in the pure deterministic structure and the slowest in the pure stochastic structure. Among the three designs, the pure

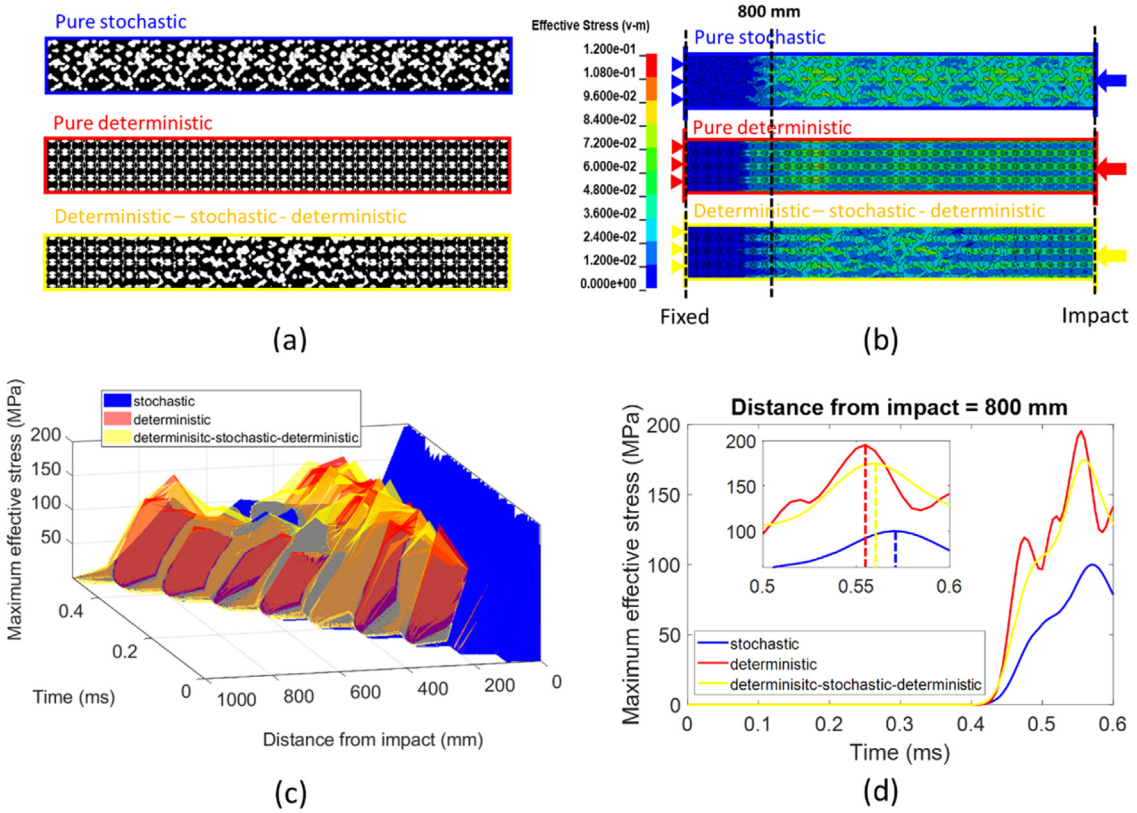

Fig. 10. Comparison among three structure designs: stochastic, deterministic, and stochastically graded. (a) Structural images of pure stochastic, pure deterministic, determinisitc-stochastic-deterministic structure. (b) Stress contours of the pure stochastic, pure deterministic, deterministic-stochastic-deterministic structures at time = 0.485 ms. (c) Time-distance-stress plot for pure stochastic, pure deterministic, deterministic-stochastic-deterministic structure. (d) Time-maximum effective stress plot at 800 mm from impact end.

deterministic structure has the highest effective stress peak, and the pure stochastic structure has the lowest effective stress peak. The mixed stochasticity structure design is in-between. We also observe that a higher structure stochasticity leads to a flatter distribution of stresses inside the structure, thus reducing the stress-induced failures in microstructure. As shown in Fig. 10(d) and Fig. A3(c), we can tailor the gradient of the time-maximum effective stress curve by arranging the local stochasticity differently. Potential applications of the stochastically graded structures include functional structures with tailorable anisotropicity, programmable metamaterials controlling stress wave propagation, and bio-compatible metamaterials.

7. Conclusion and future work

We present a deep generative design approach that tailors the microstructure morphology to achieve desired microstructure properties and structural stochasticity. We establish a highly diverse database including various types of deterministic and stochastic high-resolution microstructure images. A Fourier spectrum-based metric is proposed to provide a quantitative measurement of the structural stochasticity. A property-aware deep generative model is proposed to obtain a unified, continuous feature space that embodies microstructure features ranging from deterministic to stochastic, as well as an effective predictor of the microstructure-property relationship. With the unified feature space as the design space, we propose a novel microstructure method for stochasticity and property, where we morph a stochastic microstructure (start point) continuously into a deterministic microstructure with desired properties, or vice versa. We propose to create stochastically graded structures by assembling the microstructure building blocks with different structural stochasticity levels. We demonstrate the possibility of manipulating stress wave propagation behaviors by varying the local stochasticity of the structure while maintaining the static performances. In the future work, we will extend the proposed method to 3D microstructure design and propose a systematic approach for optimizing the stochastically graded microstructures. We will also improve the deep generative model by incorporating more geometrical constraints, such as the connectivity of a certain material phase, to guarantee a good manufacturability of the microstructure designs.

Data availability

Data will be made available on request.

Declaration of Competing Interest

The authors declare that they have no known competing financial interests or personal relationships that could have appeared to influence the work reported in this paper.

Acknowledgements

The authors gratefully acknowledge financial support from the National Science Foundation (CAREER Award CMMI-2142290).

Appendix

Finite element simulation: Simulation of the microstructure's elastic properties are implemented in ABAQUS. The 2D microstructures have the dimension of 128 mm × 128 mm. The pixel mesh size is 1 mm × 1 mm, and the elastic moduli and Poisson's ratio are consistent with the design cases. Unified periodical boundary conditions are applied to predict all elastic constants of the microstructure. The stress–strain relation of the 2D microstructure can be written as:

$$\left[\bar{\boldsymbol{\varepsilon}}\right] = [\boldsymbol{S}]\left[\bar{\boldsymbol{\sigma}}\right] \tag{A1}$$

where $[\boldsymbol{S}]$ is the compliance matrix,

$$[S] = \begin{bmatrix} S_{11} & S_{12} & 0 \\ S_{12} & S_{22} & 0 \\ 0 & 0 & S_{66} \end{bmatrix} \tag{A2}$$

$[S]$ is extracted from the ABAQUS simulation results (Fig. A2). The relations between the engineering elastic constants and S_{ij} are:

$$E_x = \frac{1}{S_{11}} E_y = \frac{1}{S_{22}} \nu = -\frac{S_{12}}{S_{11}} G = \frac{1}{S_{66}} \tag{A3}$$

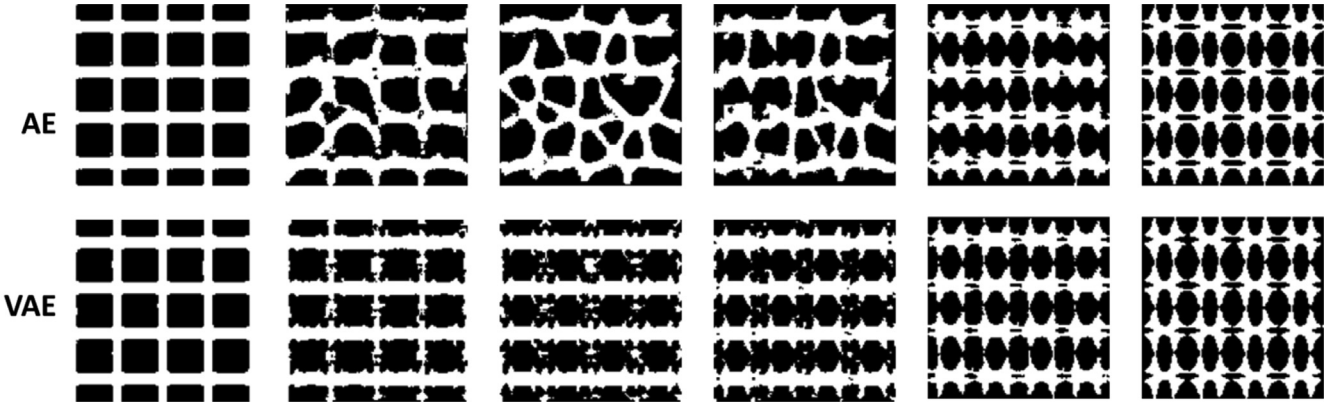

Fig. A1. Linear interpolation between two deterministic microstructures for AE and VAE. For AE, the intermediate point between two deterministic microstructure samples in the latent space might be a stochastic microstructure that does not resemble the two original designs. For VAE, the intermediate points between two deterministic microstructure samples are also deterministic or close to deterministic.

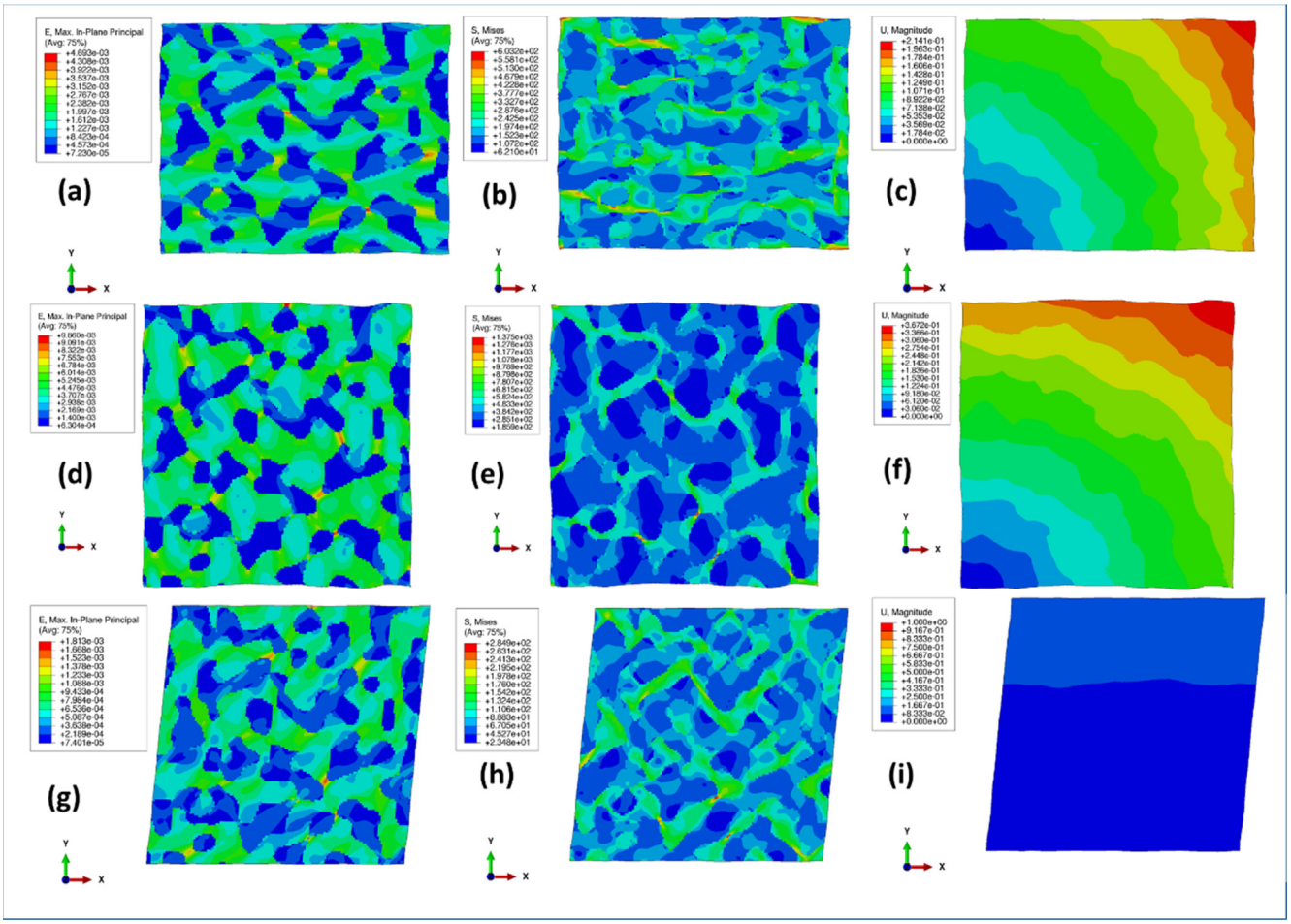

Fig. A2. Elasticity property analysis on a heterogeneous microstructure. (a), (d), (g) Maximum In-Plane Strain on x-direction, y-direction, and shearing, (b)(e)(h) Maximum von Mises stress on x-direction, y-direction, and shearing, (c)(f)(i) Maximum displacement on x-direction, y-direction, and shearing. The deformation scale factor is set as 100 to display the deformation.

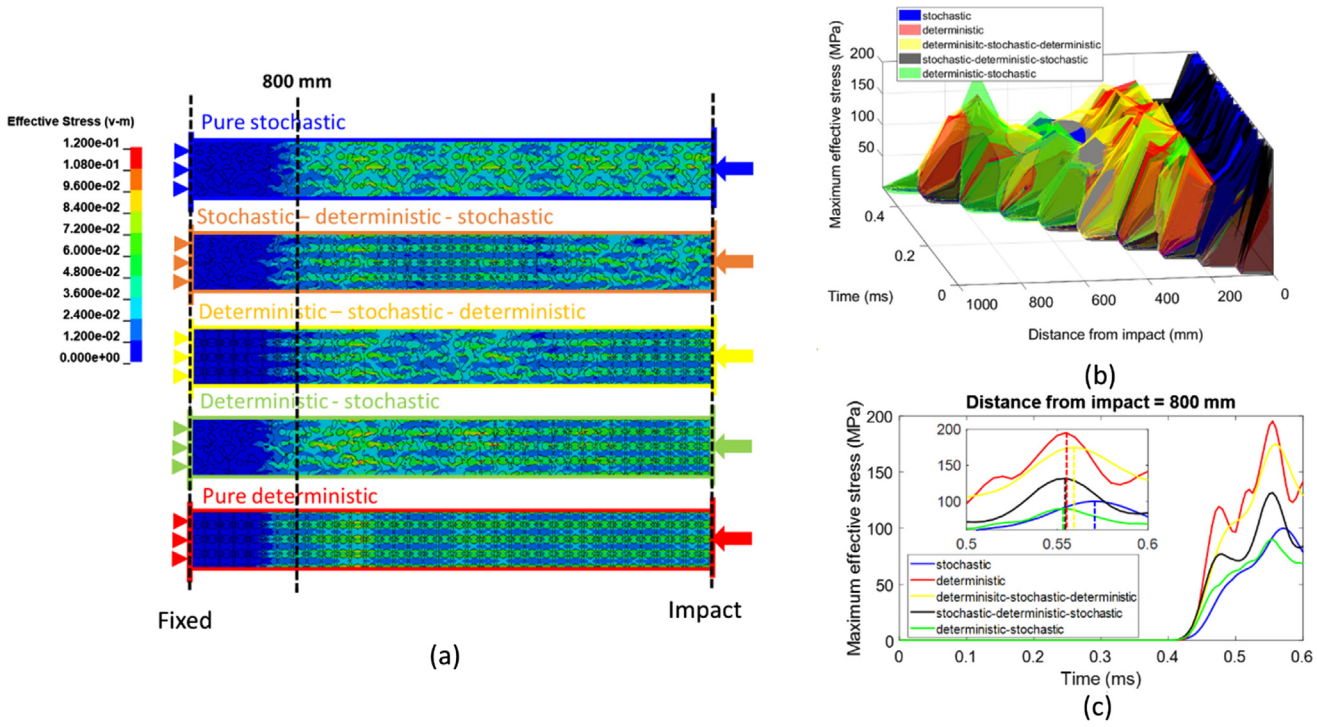

Fig. A3. (a) Stress wave in pure stochastic, stochastic-deterministic-stochastic, deterministic-stochastic-deterministic, deterministic-stochastic, and pure deterministic structure at time = 0.485 ms. (b) Time-distance-maximum effective stress plot for pure stochastic, stochastic-deterministic-stochastic, deterministic-stochastic-deterministic, deterministic-stochastic, and pure deterministic structure. (c) Time-maximum effective stress plot at 800 mm from impact end.

Appendix A. Supplementary material

Supplementary data to this article can be found online at https://doi.org/10.1016/j.matdes.2022.111223.

References

[1] S. Hein, T. Danner, D. Westhoff, B. Prifling, R. Scurtu, L. Kremer, A. Hoffmann, A. Hilger, M. Osenberg, I. Manke, Influence of conductive additives and binder on the impedance of lithium-ion battery electrodes: effect of morphology, J. Electrochem. Soc. 167 (1) (2020) 013546.

[2] C. Huang, P.S. Grant, Coral-like directional porosity lithium ion battery cathodes by ice templating, J. Mater. Chem. A 6 (30) (2018) 14689–14699.

[3] M.D. Kok, R. Jervis, T.G. Tranter, M.A. Sadeghi, D.J. Brett, P.R. Shearing, J.T. Gostick, Mass transfer in fibrous media with varying anisotropy for flow battery electrodes: direct numerical simulations with 3D X-ray computed tomography, Chem. Eng. Sci. 196 (2019) 104–115.

[4] S. Zekoll, C. Marriner-Edwards, A.O. Hekselman, J. Kasemchainan, C. Kuss, D.E. Armstrong, D. Cai, R.J. Wallace, F.H. Richter, J.H. Thijssen, Hybrid electrolytes with 3D bicontinuous ordered ceramic and polymer microchannels for all-solid-state batteries, Energy Environ. Sci. 11 (1) (2018) 185–201.

[5] F. Wein, P.D. Dunning, J.A. Norato, A review on feature-mapping methods for structural optimization, Struct. Multidiscip. O. (2020) 1–42.

[6] J. Lepine, J.-Y. Trepanier, F. Pepin, Wing aerodynamic design using an optimized NURBS geometrical representation, in: 38th Aerospace Sciences Meeting and Exhibit, 2000, p. 669.

[7] Z. Habib, M. Sarfraz, M. Sakai, Rational cubic spline interpolation with shape control, Comput. Graphics 29 (4) (2005) 594–605.

[8] Y. Zhang, W. Wang, T.J. Hughes, Solid T-spline construction from boundary representations for genus-zero geometry, Comput. Methods Appl. Mech. Eng. 249 (2012) 185–197.

[9] M.P. Bendsøe, N. Kikuchi, Generating optimal topologies in structural design using a homogenization method, Comput. Methods Appl. Mech. Eng. 71 (2) (1988) 197–224.

[10] O. Sigmund, On the design of compliant mechanisms using topology optimization, J. Struct. Mech. 25 (4) (1997) 493–524.

[11] W. Zuo, K. Saitou, Multi-material topology optimization using ordered SIMP interpolation, Struct. Multidiscip. O. 55 (2) (2017) 477–491.

[12] M.Y. Wang, X. Wang, D. Guo, A level set method for structural topology optimization, Comput. Methods Appl. Mech. Eng. 192 (1–2) (2003) 227–246.

[13] Y. Wang, J. Gao, Z. Luo, T. Brown, N. Zhang, Level-set topology optimization for multimaterial and multifunctional mechanical metamaterials, Eng. Optim. 49 (1) (2017) 22–42.

[14] Z. Chen, T. Huang, Y. Shao, Y. Li, H. Xu, K. Avery, D. Zeng, W. Chen, X. Su, Multiscale finite element modeling of sheet molding compound (SMC) composite structure based on stochastic mesostructure reconstruction, Compos. Struct. 188 (2018) 25–38.

[15] Z. Chen, H. Tang, Y. Shao, Q. Sun, G. Zhou, Y. Li, H. Xu, D. Zeng, X. Su, Failure of chopped carbon fiber Sheet Molding Compound (SMC) composites under uniaxial tensile loading: computational prediction and experimental analysis, Compos. A Appl. Sci. Manuf. 118 (2019) 117–130.

[16] M. Ebner, F. Geldmacher, F. Marone, M. Stampanoni, V. Wood, X-ray tomography of porous, transition metal oxide based lithium ion battery electrodes, Adv. Energy Mater. 3 (7) (2013) 845–850.

[17] M. Kespe, H. Nirschl, Numerical simulation of lithium-ion battery performance considering electrode microstructure, Int. J. Energy Res. 39 (15) (2015) 2062–2074.

[18] A.N. Mistry, K. Smith, P.P. Mukherjee, Secondary-phase stochastics in lithium-ion battery electrodes, ACS Appl. Mater. Interfaces 10 (7) (2018) 6317–6326.

[19] Y. Jiao, F. Stillinger, S. Torquato, Modeling heterogeneous materials via two-point correlation functions: basic principles, Phys. Rev. E 76 (3) (2007) 031110.

[20] Y. Jiao, F.H. Stillinger, S. Torquato, Modeling heterogeneous materials via two-point correlation functions. II. Algorithmic details and applications, Phys. Rev. E 77 (3) (2008).

[21] S. Torquato, Optimal design of heterogeneous materials, Annu. Rev. Mater. Res. 40 (2010) 101–129.

[22] Y. Zhang, M. Yan, Y. Wan, Z. Jiao, Y. Chen, F. Chen, C. Xia, M. Ni, High-throughput 3D reconstruction of stochastic heterogeneous microstructures in energy storage materials, npj Comput. Mater. 5 (1) (2019) 1–8.

[23] S. Yu, C. Wang, Y. Zhang, B. Dong, Z. Jiang, X. Chen, W. Chen, C. Sun, Design of non-deterministic quasi-random nanophotonic structures using Fourier space representations, Sci. Rep. 7 (1) (2017) 1–10.

[24] A. Iyer, R. Dulal, Y. Zhang, U.F. Ghumman, T. Chien, G. Balasubramanian, W. Chen, Designing anisotropic microstructures with spectral density function, Comput. Mater. Sci. 179 (2020) 109559.

[25] J.A. Quiblier, A new 3-dimensional modeling technique for studying porous-media, J. Colloid Interf. Sci. 98 (1) (1984) 84–102.

[26] M. Grigoriu, Random field models for two-phase microstructures, J. Appl. Phys. 94 (6) (2003) 3762–3770.

[27] L. Wang, Y.-C. Chan, F. Ahmed, Z. Liu, P. Zhu, W.J.C.M.i.A.M. Chen, Engineering, Deep generative modeling for mechanistic-based learning and design of metamaterial systems, 372 (2020) 113377.

[28] Y. Mao, Q. He, X.J.S.A. Zhao, Designing complex architectured materials with generative adversarial networks, 6 (17) (2020) eaaz4169.

[29] X. Li, S. Ning, Z. Liu, Z. Yan, C. Luo, Z.J.C.M.i.A.M. Zhuang, Engineering, Designing phononic crystal with anticipated band gap through a deep learning based data-driven method, 361 (2020) 112737.

[30] W. Ma, F. Cheng, Y. Xu, Q. Wen, Y.J.A.M. Liu, Probabilistic representation and inverse design of metamaterials based on a deep generative model with semi-supervised learning strategy, 31 (35) (2019) 1901111.
[31] S.J. Pan, Q. Yang, A survey on transfer learning, IEEE Trans. Knowl. Data Eng. 22 (10) (2009) 1345–1359.
[32] Y. Bengio, Deep learning of representations for unsupervised and transfer learning, in: Proceedings of ICML workshop on unsupervised and transfer learning, 2012, pp. 17–36.
[33] A. Wei, J. Xiong, W. Yang, F. Guo, Deep learning-assisted elastic isotropy identification for architected materials, Extreme Mech. Lett. 43 (2021) 101173.
[34] J. Jung, J.I. Yoon, H.K. Park, H. Jo, H.S. Kim, Microstructure design using machine learning generated low dimensional and continuous design space, Materialia (2020) 100690.
[35] R. Cang, H. Li, H. Yao, Y. Jiao, Y. Ren, Improving direct physical properties prediction of heterogeneous materials from imaging data via convolutional neural network and a morphology-aware generative model, Comput. Mater. Sci. 150 (2018) 212–221.
[36] S. Sundar, V. Sundararaghavan, Database development and exploration of process–microstructure relationships using variational autoencoders, Mater. Today Commun. (2020) 101201.
[37] Y. Kim, H.K. Park, J. Jung, P. Asghari-Rad, S. Lee, J.Y. Kim, H.G. Jung, H.S. Kim, Exploration of optimal microstructure and mechanical properties in continuous microstructure space using a variational autoencoder, Mater. Des. 202 (2021) 109544.
[38] S. Noguchi, J. Inoue, Stochastic characterization and reconstruction of material microstructures for establishment of process-structure-property linkage using the deep generative model, Phys. Rev. E 104 (2) (2021) 025302.
[39] Z. Pei, K.A. Rozman, Ö.N. Doğan, Y. Wen, N. Gao, E.A. Holm, J.A. Hawk, D.E. Alman, M.C. Gao, Machine-learning microstructure for inverse material design, Adv. Sci. 8 (23) (2021) 2101207.
[40] Z. Yang, X. Li, L. Catherine Brinson, A.N. Choudhary, W. Chen, A. Agrawal, Microstructural materials design via deep adversarial learning methodology, J. Mech. Des. 140 (11) (2018).
[41] R.K. Tan, N.L. Zhang, W. Ye, A deep learning–based method for the design of microstructural materials, Struct. Multidiscip. Optim. (2019) 1–22.
[42] C.T. Chen, G.X. Gu, Generative deep neural networks for inverse materials design using backpropagation and active learning, Adv. Sci. (Weinh) 7 (5) (2020) 1902607.
[43] X. Li, S. Ning, Z. Liu, Z. Yan, C. Luo, Z. Zhuang, Designing phononic crystal with anticipated band gap through a deep learning based data-driven method, Comput. Method Appl. M. 361 (2020) 112737.
[44] H. Zhang, Y. Wang, H. Zhao, K. Lu, D. Yu, J. Wen, Accelerated topological design of metaporous materials of broadband sound absorption performance by generative adversarial networks, Mater. Des. 207 (2021) 109855.
[45] H.T. Kollmann, D.W. Abueidda, S. Koric, E. Guleryuz, N.A. Sobh, Deep learning for topology optimization of 2D metamaterials, Mater. Des. 196 (2020) 109098.
[46] X. Zheng, T.-T. Chen, X. Guo, S. Samitsu, I. Watanabe, Controllable inverse design of auxetic metamaterials using deep learning, Mater. Des. 211 (2021) 110178.
[47] A. Samaei, S. Chaudhuri, Mechanical performance of zirconia-silica bilayer coating on aluminum alloys with varying porosities: deep learning and microstructure-based FEM, Mater. Des. 207 (2021) 109860.
[48] H. Xu, D.A. Dikin, C. Burkhart, W. Chen, Descriptor-based methodology for statistical characterization and 3D reconstruction of microstructural materials, Comput. Mater. Sci. 85 (2014) 206–216.
[49] M. Yang, A. Nagarajan, B. Liang, S. Soghrati, New algorithms for virtual reconstruction of heterogeneous microstructures, Comput. Methods Appl. Mech. Eng. 338 (2018) 275–298.
[50] S. Hein, J. Feinauer, D. Westhoff, I. Manke, V. Schmidt, A. Latz, Stochastic microstructure modeling and electrochemical simulation of lithium-ion cell anodes in 3D, J. Power Sources 336 (2016) 161–171.
[51] Y. Li, Z. Chen, L. Su, W. Chen, X. Jin, H. Xu, Stochastic reconstruction and microstructure modeling of SMC chopped fiber composites, Compos. Struct. 200 (2018) 153–164.
[52] S. Falco, J. Jiang, F. De Cola, N. Petrinic, Generation of 3D polycrystalline microstructures with a conditioned Laguerre-Voronoi tessellation technique, Comput. Mater. Sci. 136 (2017) 20–28.
[53] S. Yu, Y. Zhang, C. Wang, W.-K. Lee, B. Dong, T.W. Odom, C. Sun, W. Chen, Characterization and design of functional quasi-random nanostructured materials using spectral density function, J. Mech. Des. 139 (7) (2017) 071401.
[54] L. Wang, Y.-C. Chan, F. Ahmed, Z. Liu, P. Zhu, W. Chen, Deep generative modeling for mechanistic-based learning and design of metamaterial systems, Comput. Methods Appl. Mech. Eng. 372 (2020) 113377.
[55] L. Wang, Y.-C. Chan, Z. Liu, P. Zhu, W. Chen, Data-driven metamaterial design with Laplace-Beltrami spectrum as "shape-DNA", Struct. Multidiscip. Optim. 61 (6) (2020) 2613–2628.
[56] P. Vogiatzis, S. Chen, X.D. Gu, C.-H. Chuang, H. Xu, N. Lei, Multi-material topology optimization of structures infilled with conformal metamaterials, in: ASME 2018 International Design Engineering Technical Conferences and Computers and Information in Engineering Conference, American Society of Mechanical Engineers, 2018, pp. V02BT03A009-V02BT03A009.
[57] M. Ding, S. Yin, D. Chen, J. Zhong, Y. Ni, C. Lu, Z. Xu, Z. Ji, Hexagonal NaYF4: Yb3+/Er3+ nano/micro-structures: controlled hydrothermal synthesis and morphology-dependent upconversion luminescence, Appl. Surf. Sci. 333 (2015) 23–33.
[58] R. Xu, Y. Yang, F. Yin, P. Liu, P. Cloetens, Y. Liu, F. Lin, K. Zhao, Heterogeneous damage in Li-ion batteries: experimental analysis and theoretical modeling, J. Mech. Phys. Solids 129 (2019) 160–183.
[59] S. Coertjens, R. De Dier, P. Moldenaers, L. Isa, J. Vermant, Adsorption of ellipsoidal particles at liquid–liquid interfaces, Langmuir 33 (11) (2017) 2689–2697.
[60] O.M. González, A. Velín, A. García, C.R. Arroyo, H.L. Barrigas, K. Vizuete, A. Debut, Representative hardwood and softwood green tissue-microstructure transitions per age group and their inherent relationships with physical-mechanical properties and potential applications, Forests 11 (5) (2020) 569.
[61] L. Song, Y. Song, C. Xiao, L. Tianhua, G. Zhuang, W. Deping, OH− ions-controlled synthesis and upconversion luminescence properties of NaYF4: Yb3+, Er3+ nanocrystals via oleic acid-assisted hydrothermal process, J. Rare Earths 35 (8) (2017) 753–760.
[62] H. Qiu, G. Chen, L. Sun, S. Hao, G. Han, C. Yang, Ethylenediaminetetraacetic acid (EDTA)-controlled synthesis of multicolor lanthanide doped BaYF 5 upconversion nanocrystals, J. Mater. Chem. 21 (43) (2011) 17202–17208.
[63] X. Lu, A. Bertei, D.P. Finegan, C. Tan, S.R. Daemi, J.S. Weaving, K.B. O'Regan, T. M. Heenan, G. Hinds, E. Kendrick, 3D microstructure design of lithium-ion battery electrodes assisted by X-ray nano-computed tomography and modelling, Nat. Commun. 11 (1) (2020) 1–13.
[64] P.J. Bishop, S.A. Hocknull, C.J. Clemente, J.R. Hutchinson, A.A. Farke, B.R. Beck, R.S. Barrett, D.G. Lloyd, Cancellous bone and theropod dinosaur locomotion. Part I—an examination of cancellous bone architecture in the hindlimb bones of theropods, PeerJ 6 (2018) e5778.
[65] M. Ebner, D.W. Chung, R.E. García, V. Wood, Tortuosity anisotropy in lithium-ion battery electrodes, Adv. Energy Mater. 4 (5) (2014) 1301278.
[66] R. Bostanabad, Y. Zhang, X. Li, T. Kearney, L.C. Brinson, D.W. Apley, W.K. Liu, W. Chen, Computational microstructure characterization and reconstruction: review of the state-of-the-art techniques, Prog. Mater. Sci. 95 (2018) 1–41.
[67] H. Xu, Y. Li, C. Brinson, W. Chen, A descriptor-based design methodology for developing heterogeneous microstructural materials system, J. Mech. Des. 136 (5) (2014) 051007.
[68] H. Xu, J. Zhu, D.P. Finegan, H. Zhao, X. Lu, W. Li, N. Hoffman, A. Bertei, P. Shearing, M.Z. Bazant, Guiding the design of heterogeneous electrode microstructures for Li-Ion batteries: microscopic imaging, predictive modeling, and machine learning, Adv. Energy Mater. 11 (19) (2021) 2003908.
[69] C. Chatfield, H. Xing, The Analysis of Time Series: An Introduction with R, CRC press, 2019.
[70] N. Berk, Scattering properties of a model bicontinuous structure with a well defined length scale, Phys. Rev. Lett. 58 (25) (1987) 2718.
[71] S. Torquato, G. Stell, Microstructure of two-phase random media. I. The n-point probability functions, J. Chem. Phys. 77 (4) (1982) 2071–2077.
[72] C. Yeong, S. Torquato, Reconstructing random media, Phys. Rev. E 57 (1) (1998) 495.
[73] N. Wiener, Generalized harmonic analysis, Acta Mathematica 55 (1) (1930) 117–258.
[74] Z. Xia, Y. Zhang, F. Ellyin, A unified periodical boundary conditions for representative volume elements of composites and applications, Int. J. Solids Struct. 40 (8) (2003) 1907–1921.
[75] L. Weng, From gan to wgan, arXiv preprint arXiv:1904.08994 (2019).
[76] D. Bau, J.-Y. Zhu, J. Wulff, W. Peebles, H. Strobelt, B. Zhou, A. Torralba, Seeing what a gan cannot generate, in: Proceedings of the IEEE/CVF International Conference on Computer Vision, 2019, pp. 4502–4511.
[77] W. Ma, F. Cheng, Y. Xu, Q. Wen, Y. Liu, Probabilistic representation and inverse design of metamaterials based on a deep generative model with semi-supervised learning strategy, Adv. Mater. 31 (35) (2019) 1901111.
[78] Z. Wang, W. Xian, M.R. Baccouche, H. Lanzerath, Y. Li, H. Xu, Design of phononic bandgap metamaterials based on gaussian mixture beta variational autoencoder and iterative model updating, J. Mech. Des. (2022) 1–35.
[79] X. Li, Y. Zhang, H. Zhao, C. Burkhart, L.C. Brinson, W. Chen, A transfer learning approach for microstructure reconstruction and structure-property predictions, Sci. Rep. 8 (1) (2018) 1–13.
[80] K. Simonyan, A. Zisserman, Very deep convolutional networks for large-scale image recognition, arXiv preprint arXiv:1409.1556 (2014).
[81] R. Bostanabad, Reconstruction of 3D microstructures from 2D images via transfer learning, Comput. Aided Des. 128 (2020) 102906.
[82] A. Makhzani, J. Shlens, N. Jaitly, I. Goodfellow, B. Frey, Adversarial autoencoders, arXiv preprint arXiv:1511.05644 (2015).
[83] L. Van der Maaten, G. Hinton, Visualizing data using t-SNE, J. Machine Learning Res. 9 (11) (2008).
[84] S. Ruder, An overview of gradient descent optimization algorithms, arXiv preprint arXiv:1609.04747 (2016).
[85] E. Polak, Optimization: Algorithms and Consistent Approximations, Springer Science & Business Media, 2012.
[86] T. Bäck, H.-P. Schwefel, An overview of evolutionary algorithms for parameter optimization, Evol. Comput. 1 (1) (1993) 1–23.
[87] M. Mitchell, An Introduction to Genetic Algorithms, MIT press, 1998.
[88] S. Sivanandam, S. Deepa, Genetic Algorithms, Introduction to Genetic Algorithms, Springer, 2008, pp. 15–37.

[89] R. Hull, P. Keblinski, D. Lewis, A. Maniatty, V. Meunier, A.A. Oberai, C.R. Picu, J. Samuel, M.S. Shephard, M. Tomozawa, Stochasticity in materials structure, properties, and processing—a review, Appl. Phys. Rev. 5 (1) (2018) 011302.
[90] V. Deimede, C. Elmasides, Separators for lithium-ion batteries: a review on the production processes and recent developments, Energy Technol. 3 (5) (2015) 453–468.
[91] J. Yang, C.K. Soh, Structural optimization by genetic algorithms with tournament selection, J. Comput. Civil Eng. 11 (3) (1997) 195–200.
[92] B.L. Miller, D.E. Goldberg, Genetic algorithms, tournament selection, and the effects of noise, Complex systems 9 (3) (1995) 193–212.
[93] K. Deb, A. Pratap, S. Agarwal, T. Meyarivan, A fast and elitist multiobjective genetic algorithm: NSGA-II, IEEE Trans. Evol. Comput. 6 (2) (2002) 182–197.
[94] J. Blank, K. Deb, Pymoo: multi-objective optimization in python, IEEE Access 8 (2020) 89497–89509.
[95] K. Kira, L.A. Rendell, The feature selection problem: traditional methods and a new algorithm, Aaai (1992) 129–134.
[96] I. Kononenko, Estimating attributes: analysis and extensions of RELIEF, in: European Conference on Machine Learning, Springer, 1994, pp. 171–182.
[97] M. Robnik-Šikonja, I. Kononenko, An adaptation of Relief for attribute estimation in regression, in: Machine Learning: Proceedings of the Fourteenth International Conference (ICML'97), 1997, pp. 296–304.
[98] H. Xu, R. Liu, A. Choudhary, W. Chen, A machine learning-based design representation method for designing heterogeneous microstructures, J. Mech. Des. 137 (5) (2015) 051403.
[99] A. Emamian, S.F. Corbin, A. Khajepour, In-situ deposition of metal matrix composite in Fe-Ti-C system using laser cladding process, Metal, Ceramic and Polymeric Composites for Various Uses, IntechOpen2011.
[100] Y. Wu, Y. Wang, F. Yang, Comparison of multilayer transparent wood and single layer transparent wood with the same thickness, Front. Mater. 8 (2021) 41.
[101] L. Liu, Y. Zhou, S. Pan, Experimental and analysis of the mechanical behaviors of multi-walled nanotubes/polyurethane nanoweb-reinforced epoxy composites, J. Reinf. Plast. Compos. 32 (11) (2013) 823–834.
[102] Y. Wu, Y. Wang, F. Yang, Comparison of multilayer transparent wood and single layer transparent wood with the same thickness, Front. Mater. 8 (2021) 633345.
[103] P. Elia, E. Nativ-Roth, Y. Zeiri, Z.e. Porat, Determination of the average pore-size and total porosity in porous silicon layers by image processing of SEM micrographs, Microporous Mesoporous Mater. 225 (2016) 465–471.

Supporting Material

Harness the Structural Stochasticity in Computational Discovery and Design of Microstructural Materials

*Leidong Xu, Nathaniel Hoffman, Zihan Wang and Hongyi Xu**

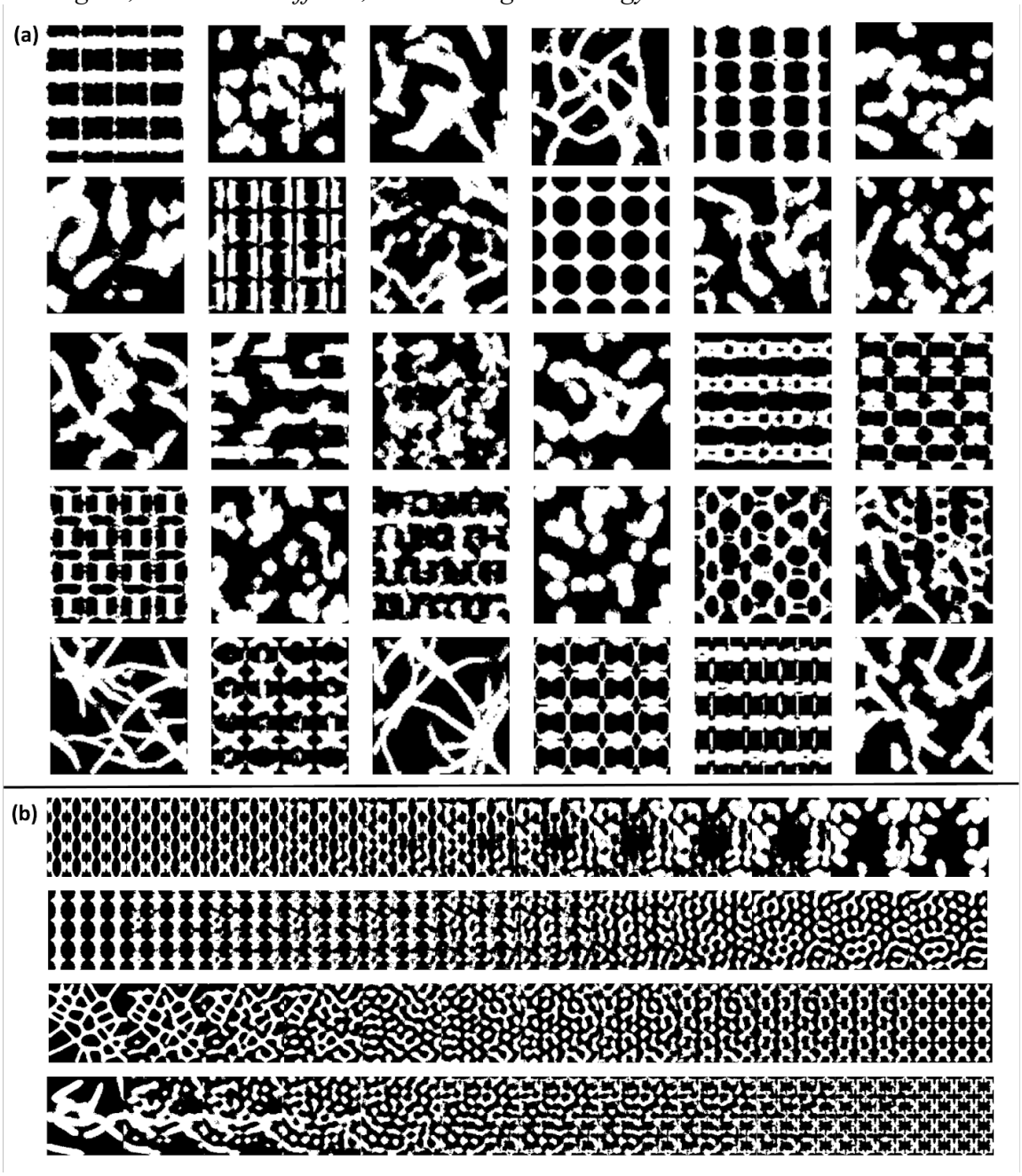

Figure S1. (a) Synthetic microstructures by sampling latent feature values from a standard Normal distribution. (b) Examples of smooth transition from a deterministic (periodic) microstructure to a stochastic microstructure, or vice versa.

Table S1. The dimensionality of each layer in the proposed deep learning model architecture.

Block	Specifications
Encoder Conv-1	(Conv64 + BatchNorm+ ReLU) ×2 + Max Pooling
Encoder Conv-2	(Conv128 + BatchNorm+ ReLU) ×3 + Max Pooling
Encoder Conv-3	(Conv256 + BatchNorm+ ReLU) ×3 + Max Pooling
Encoder Conv-4	(Conv512 + BatchNorm+ ReLU) ×3
Encoder FC	2000+ReLU->1000+ReLU->100
Mean, Variance, Latent vector	100
Decoder FC	100+ReLU->500+ReLU->2000
Decoder Conv-1	(Conv512 + BatchNorm+ ReLU) ×3 + UpSampling
Decoder Conv-2	(Conv256 + BatchNorm+ ReLU) ×3 + UpSampling
Decoder Conv-3	(Conv128 + BatchNorm+ ReLU) ×3 + UpSampling
Decoder Conv-4	(Conv64 + BatchNorm+ ReLU) ×2 + Conv1+Sigmoid
DNN Regressor	(1000+BatchNorm+ReLU) ×2+(500+ReLU) ×2+100
Discriminator(AAE ONLY)	(1000+BatchNorm+LeakyReLU) ×2 +(500+BatchNorm+LeakyReLU) ×2 +(100+BatchNorm+LeakyReLU) ×2+Sigmoid

Table S2. Detailed material properties used in simulations. For the boron phase, *MAT_ELASTIC material card is used; for the aluminum phase, *MAT_PIECEWISE_LINEAR_PLASTICITY material card is used.

	Density	Young's Modulus	Yield Strength	Poisson's Ratio
Boron Phase	2.34g/cm3	379300 MPa	/	0.1
Aluminum Phase	2.7 g/cm3	68300 MPa	276 MPa	0.3

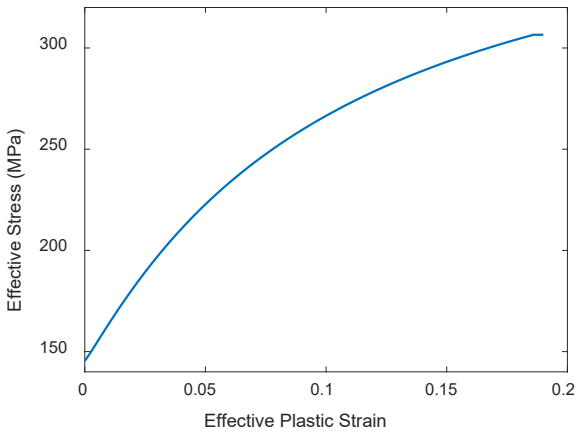

Figure S2: Effective stress versus effective plastic strain of aluminum phase used in simulations.

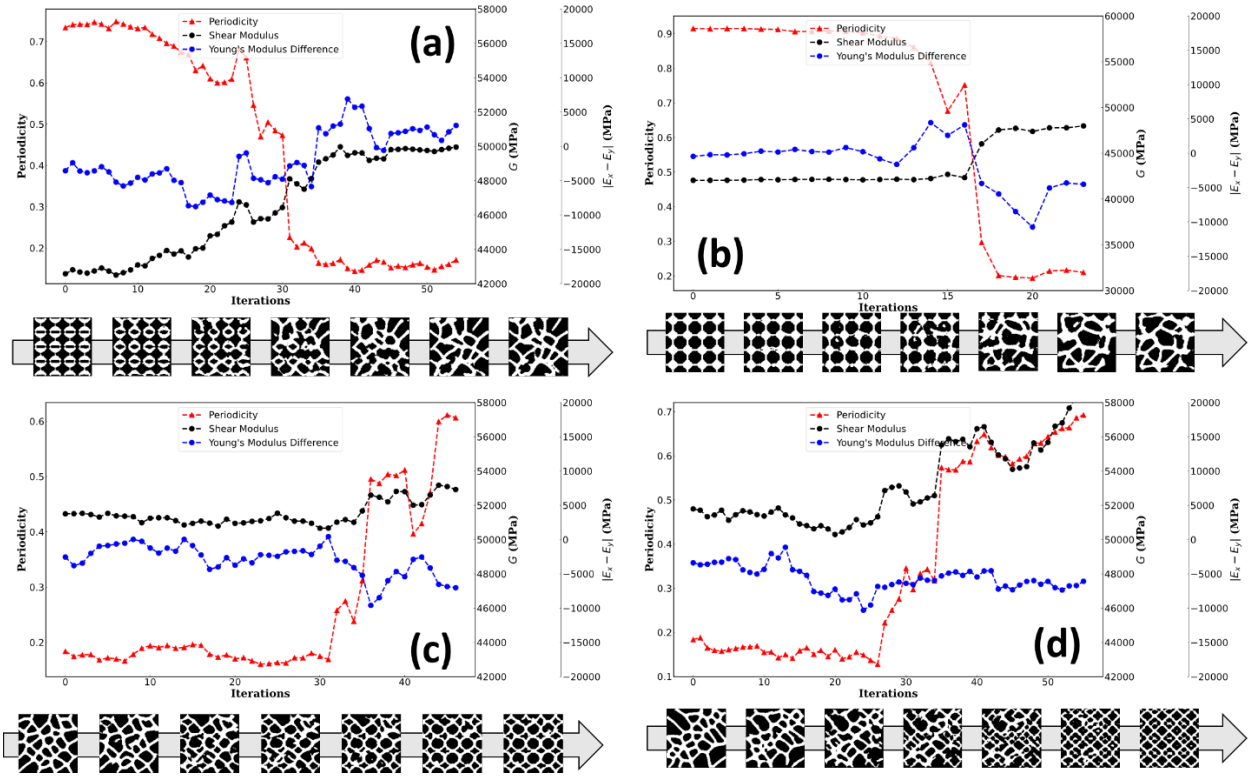

Figure S3: More microstructure design cases. (a) and (b): Search stochastic designs with maximum shear modulus and equivalent Young's modulus along x- and y-direction, using a deterministic design as the start point of search. (c) and (d): Search deterministic (periodic) designs with maximum shear modulus and equivalent Young's modulus along x- and y-direction, using a stochastic design as the start point of search.

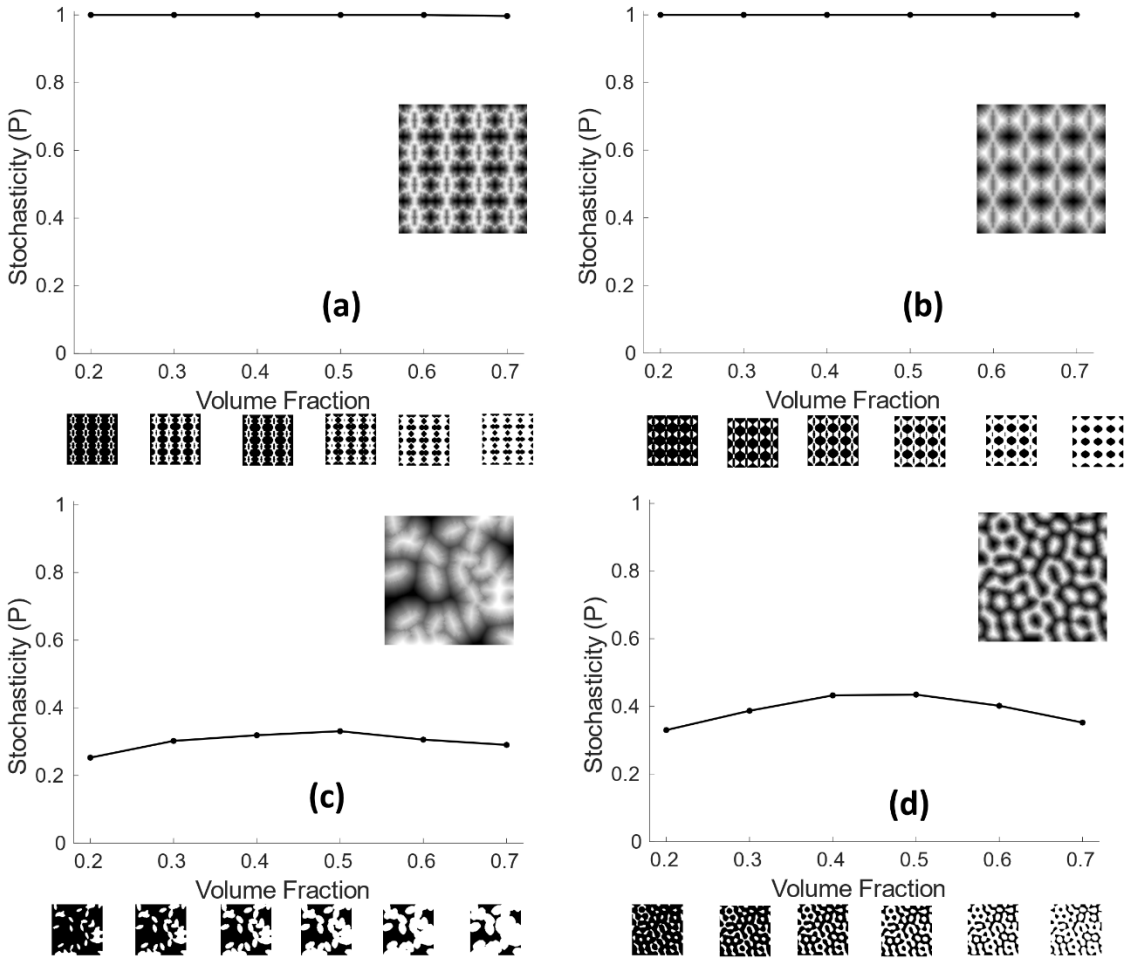

Figure S4: Stochasticity metric values of binary microstructure images with different volume fraction values. In each subplot, the binary images are obtained from the same greyscale master image.

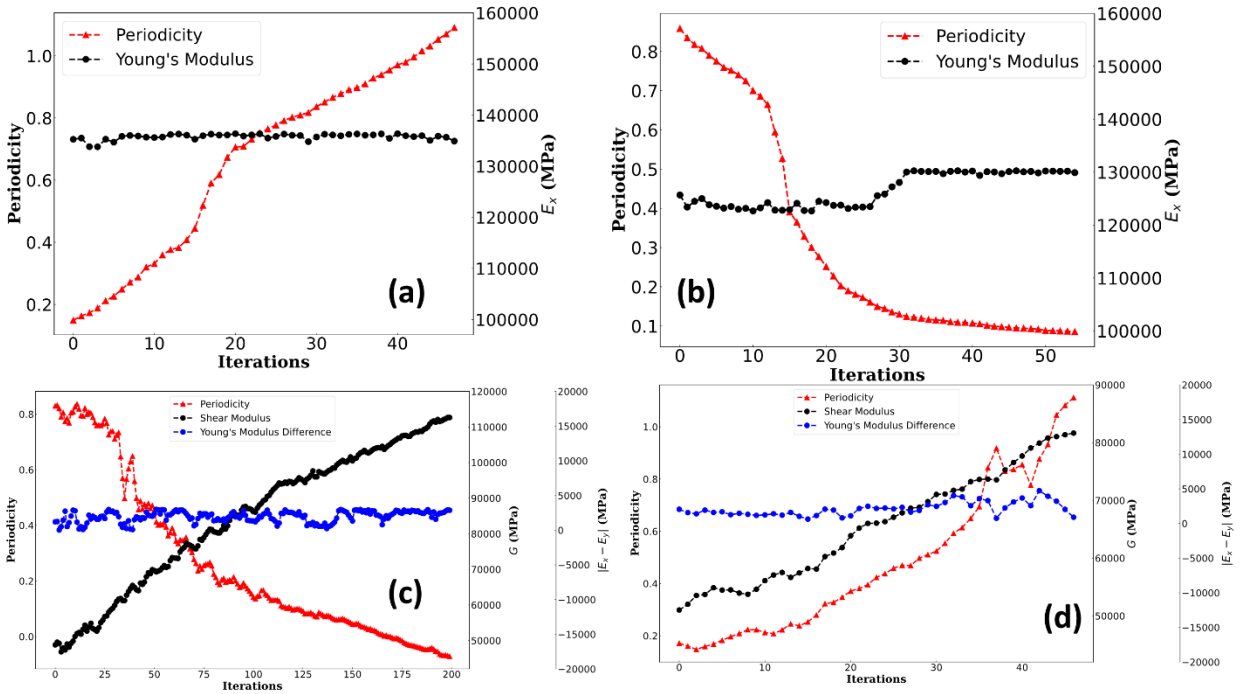

Figure S5: Optimization history plots using the regressor-predicted properties for Design case 1 and 2. In Figure 9 of the manuscript, the optimization history plots are created using the true properties of all designs generated in the design process. In this figure, the optimization history plots are created using the properties predicted by the regressors. The subplots in this figure corespond to Figure 9 (a), (b), (c), and (d) in the manuscript, respectively.

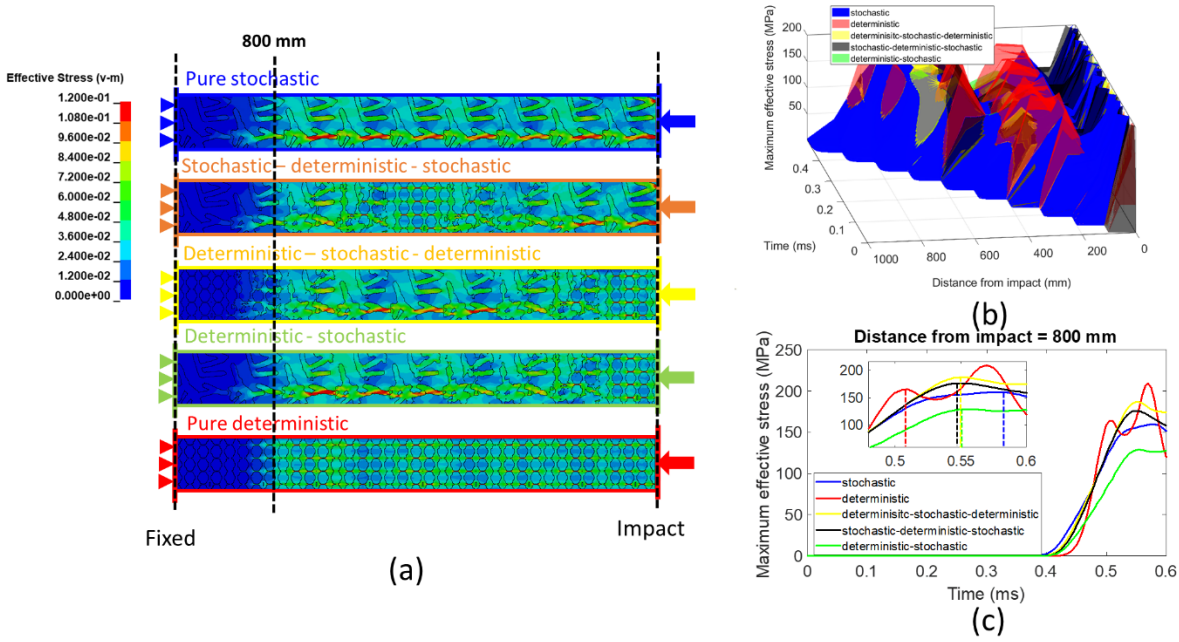

Figure S6: Another example of the stochastically graded structure design. (a) Stress contours of the pure stochastic, stochastic-deterministic-stochastic, deterministic-stochastic-deterministic, deterministic-stochastic, and pure deterministic structures at time = 0.485 ms. (b) Time-distance-maximum effective stress plot for pure stochastic, stochastic-deterministic-stochastic, deterministic-stochastic-deterministic, deterministic-stochastic, and pure deterministic structure. (c) Comparison of the time reaching the first effective stress peak at the location of 800 mm from impact end.